Antecedent North Pacific Jet Regimes Conducive to the Development of Continental U.S. Extreme Temperature Events during the Cool Season

By

ANDREW C. WINTERS[1*], LANCE F. BOSART[1], and DANIEL KEYSER[1]

[1]Department of Atmospheric and Environmental Sciences
University at Albany – State University of New York
Albany, NY 12222

Submitted for publication in _____
XX XXX 2018

[*] *Corresponding author address:* Andrew C. Winters, Dept. of Atmospheric and Environmental Sciences, University at Albany, SUNY, 1400 Washington Ave., Albany, NY 12222. E-mail: acwinters@albany.edu

ABSTRACT

This study considers the development of continental U.S. extreme temperature events (ETEs) during the cool season (Sep–May), where extreme temperatures are defined in terms of percentiles and events are defined in terms of the spatial coverage of extreme temperatures. Following their identification, ETEs are classified into geographic clusters and stratified based on the state of the North Pacific jet (NPJ) stream prior to ETE initiation using an NPJ Phase Diagram. The NPJ Phase Diagram is developed from the two leading modes of NPJ variability during the cool season. The first mode corresponds to a zonal extension or retraction of the exit region of the climatological NPJ, while the second mode corresponds to a poleward or equatorward shift of the exit region of the climatological NPJ.

The projection of 250-hPa zonal wind anomalies onto the NPJ Phase Diagram provides an objective characterization of the state and evolution of the upper-tropospheric flow pattern over the North Pacific prior to ETEs. The analysis indicates that the preferred state and evolution of the NPJ prior to ETEs varies considerably based on the location of ETE initiation and meteorological season. The NPJ Phase Diagram is employed further to examine the synoptic-scale flow evolution that is most conducive to the initiation of southern Plains extreme warm events via composite analysis. The composite analysis demonstrates that a retracted NPJ supports an amplification of the upper-tropospheric flow pattern over North America, which subsequently induces persistent warm-air advection over the southern Plains prior to ETE initiation.

1. Introduction

The occurrence of extreme temperature events (ETEs) during the cool season (Sep–May) is often accompanied by considerable societal and economic impacts. Extreme cold events, in particular, are responsible for about 30 deaths per year in the United States (Cellitti et al. 2006), can result in substantial damage to infrastructure, and can induce agricultural and economic losses (e.g., Rogers and Rohli 1991; Gu et al. 2008; Dole et al. 2014; Wolter et al. 2015). While extreme warm events during the cool season have received less consideration within the refereed literature, they also pose considerable risks. These risks include the development of floods and ice jams on waterways due to rapid snow and ice melt, economic losses for industries reliant upon wintry conditions, and the potential loss of early-season agricultural products when an extreme warm event is followed by a hard freeze (e.g., Rogers and Rohli 1991; Gu et al. 2008; Westby et al. 2013; Dole et al. 2014; Peterson and Abatzoglou 2014; Westby and Black 2015).

From a climatological perspective, the development of one or several ETEs during a single season can contribute disproportionately to temperature anomaly statistics for that particular season (e.g., Hoerling et al. 2013; Peterson et al. 2013; Dole et al. 2014; Hartmann 2015; Wolter et al. 2015). The disproportionate contribution of ETEs to seasonal temperature anomaly statistics suggests that ETEs need to be considered in order to understand the dynamical and thermodynamic processes that operate at the weather–climate intersection. Such investigations of ETEs are of additional importance given projected changes in the frequency of ETEs within a future climate (e.g., Walsh et al. 2001; Meehl and Tebaldi 2004; Portis et al. 2006; Vavrus et al. 2006; Peterson et al. 2013; Westby et al. 2013; Scherer and Diffenbaugh 2014; Grotjahn et al. 2016).

Motivated to understand the large-scale flow patterns associated with the development of

ETEs, numerous studies have sought a relationship between cool season ETEs over North America and modes of intraannual climate variability. For example, prior work has identified relationships between ETEs and the phase of the Pacific–North American pattern (PNA; e.g., Rogers and Rohli 1991; Downton and Miller 1993; Cellitti et al. 2006; Westby et al. 2013; Loikith and Broccoli 2014; Westby and Black 2015), the North Atlantic Oscillation (NAO; e.g., Downton and Miller 1993; Cellitti et al. 2006; Kenyon and Hegerl 2008; Guirguis et al. 2011; Westby et al. 2013, Westby and Black 2015), and the Arctic Oscillation (AO; e.g., Higgins et al. 2002; Lim and Schubert 2011; Loikith and Broccoli 2014). Cool season ETEs have also been related to modes of interannual climate variability such as the phase of the Pacific Decadal Oscillation (PDO; e.g., Guirguis et al. 2011; Westby et al. 2013; Xie et al. 2017) and the El Niño–Southern Oscillation (ENSO; e.g., Higgins et al. 2002; Carrera et al. 2004; Meehl et al. 2007; Kenyon and Hegerl 2008; Guirguis et al. 2011; Lim and Schubert 2011; Westby et al. 2013; Loikith and Broccoli 2014; Xie et al. 2017). Considered together, knowledge of these relationships adds considerable value to subseasonal and seasonal forecasts of ETEs.

In addition to the relationships between cool season ETEs and modes of climate variability, Loikith and Broccoli (2014) emphasize that the synoptic-scale flow pattern also plays an important role in the development of ETEs, especially during the boreal winter. In particular, regional case studies and composite analyses of cool season ETEs over North America have identified elements of the synoptic-scale flow pattern that are often associated with the development of ETEs. Common elements among these studies include an amplified upper-tropospheric flow pattern over North America (e.g., Dallavalle and Bosart 1975; Hartjenstein and Bleck 1991; Colle and Mass 1995; Konrad 1996; Cellitti et al. 2006; Loikith and Broccoli 2012; Westby and Black 2015; Xie et al. 2017), the development of surface cyclones and anticyclones

118 that facilitate the transport of anomalous temperature into a region (e.g., Dallavalle and Bosart
119 1975; Colucci and Davenport 1987; Konrad and Colucci 1989; Colle and Mass 1995; Konrad
120 1996; Walsh et al. 2001; Grotjahn and Zhang 2017; Xie et al. 2017), and topographical effects
121 such as cold-air damming and the adiabatic warming of air parcels induced by lee subsidence
122 (e.g., Bell and Bosart 1988; Hartjenstein and Bleck 1991; Colle and Mass 1995; Brewer et al.
123 2012, 2013). Thermodynamic factors such as antecedent precipitation and soil moisture (e.g.,
124 Turner and Gyakum 2011; Brewer et al. 2013; Hoerling et al. 2013; Dole et al. 2014), as well as
125 adiabatic and diabatic processes occurring along air parcel trajectories in the absence of
126 topography (e.g., Konrad and Colucci 1989; Walsh et al. 2001; Portis et al, 2006; Turner and
127 Gyakum 2011) also play important roles in the development of ETEs.
128 While the synoptic-scale flow patterns associated with cool season ETEs feature common
129 elements, it is apparent that the structure and evolution of these flow patterns are highly
130 dependent on the location of the ETE and the meteorological season (e.g., Loikith and Broccoli
131 2012, 2014; Westby et al. 2013; Westby and Black 2015; Grotjahn et al. 2016; Grotjahn and
132 Zhang 2017; Loikith et al. 2017; Xie et al. 2017). On the basis of this observation, Grotjahn et al.
133 (2016) emphasize in their review of large-scale meteorological patterns (LSMPs) associated with
134 ETEs that additional work is required (1) to determine whether more than one type of LSMP is
135 conducive to the development of ETEs in a particular geographic region and, (2) to increase
136 understanding of the synoptic-dynamic mechanisms that support the development of LSMPs
137 associated with ETEs. These two recommendations motivate the present study.
138 Prior work on extreme weather events (EWEs) over North America has demonstrated that
139 the state and evolution of the North Pacific jet (NPJ) stream plays an important role in
140 establishing a downstream environment that is conducive to EWEs (e.g., Cordeira and Bosart

141 2010; Bosart et al. 2017). Consequently, this study addresses the two recommendations from
142 Grotjahn et al. (2016) by adopting an objective NPJ-centered framework to determine the
143 configurations of the NPJ, or NPJ regimes, that are conducive to the development of continental
144 U.S. ETEs. In particular, the adoption of this framework permits an examination of the degree to
145 which the preferred NPJ configurations prior to ETEs differ depending on the location of the
146 ETE within the continental U.S. and the meteorological season.

147 The remainder of this manuscript is structured as follows. Section 2 introduces an
148 identification scheme for continental U.S. ETEs as well as an NPJ Phase Diagram that will be
149 used to characterize the state and evolution of the NPJ prior to the development of ETEs. Section
150 3 discusses the characteristics of continental U.S. ETEs during the cool season with respect to
151 the NPJ Phase Diagram. Section 4 provides an illustrative example demonstrating how the NPJ
152 Phase Diagram can be leveraged to examine the synoptic-scale flow evolution that is most
153 conducive to the development of southern Plains extreme warm events, and section 5 offers a
154 discussion of the results.

155 **2. Methodology**

156 *a) ETE identification scheme*

157 This study employs 1-h forecasts of 2-m temperature from the National Centers for
158 Environmental Prediction Climate Forecast System Reanalysis (CFSR; Saha et al. 2010, 2014)
159 during the 36-year period, 1979–2014. The 1-h forecasts of 2-m temperature from the CFSR are
160 0.5°-resolution and are initialized every 6 h at the standard analysis times (i.e., 0000, 0600, 1200,
161 and 1800 UTC). Given that analyses of 2-m temperature are not available in the CFSR at the
162 standard analysis times, the 1-h forecasts of 2-m temperature represent a temporally continuous
163 and uniformly gridded dataset of 2-m temperatures that are suitable for identifying continental

U.S. ETEs within the CFSR during the period of study. The discussion that follows outlines the ETE identification scheme with respect to continental U.S. extreme warm events.

To identify extreme warm events, 2-m temperature distributions are constructed for each grid point at every forecast verification time during the year (i.e., 4 times daily at 0100, 0700, 1300, and 1900 UTC). A 2-m temperature distribution is constructed for a grid point at a single verification time by isolating the 2-m temperatures for that grid point at 24-h intervals within a 21-day window centered on the verification time for every year between 1979 and 2014. A 2-m temperature distribution for the 21-day window centered on 1900 UTC 30 May during 1979–2014 is provided in Fig. 1a for a grid point near Albany, NY.

The 2-m temperature distributions are then leveraged to objectively define thresholds for extreme warmth that are specific to each grid point at a particular verification time. Extreme warm temperatures are defined in this study as those temperatures that are greater than the 99th-percentile temperature for a grid point at a particular verification time. For the 2-m temperature distribution constructed for a grid point near Albany, NY, the 99th-percentile temperature is 32°C (90°F) at 1900 UTC 30 May (Fig. 1a). A horizontal distribution of the 99th-percentile temperature at 1900 UTC 30 May highlights the considerable spatial variability that characterizes the magnitude of the 99th-percentile temperature over North America (Fig. 1b).

To ensure that the identification scheme captures areas of extreme warmth that are concentrated within the same geographic region, the continental U.S. is split into two domains to the east and west of 105°W[1], respectively (Fig. 1b). For each domain, 1-h forecasts of 2-m temperature that featured at least one grid point over land with a temperature greater than its respective 99th-percentile temperature are catalogued. The catalogued 1-h forecasts of 2-m

[1] The 105°W meridian is chosen given that it parallels the easternmost extent of the Rocky Mountains, which serve as a natural geographic barrier suitable for partitioning the continental U.S.

186 temperature within each spatial domain are subsequently ranked according to the number of grid
187 points with temperatures greater than their respective 99th-percentile temperatures. Those 1-h
188 forecasts of 2-m temperature that rank in the top 5% in terms of the number of grid points
189 featuring extreme warmth are isolated and labeled as extreme warm events within that spatial
190 domain. For example, a minimum of 224 grid points must exhibit temperatures greater than their
191 respective 99th-percentile temperatures (i.e., approximately equivalent to the area enclosed within
192 a 7°×7° box) in order for a particular 1-h forecast to qualify as an extreme warm event within the
193 eastern U.S. domain (Fig. 1c). By imposing a minimum grid point threshold, the identification
194 scheme ensures that ETEs are extreme not only in terms of their temperatures but also the spatial
195 extent of those extreme temperatures.

196 Lastly, extreme warm events that occurred within 24-h of another extreme warm event
197 are considered to be the same extreme warm event and all events are classified based on the
198 meteorological season at the time of event initiation (i.e., fall, winter, spring). The identification
199 scheme for extreme warm events produces a total of 304 and 264 extreme warm events during
200 1979–2014 within the eastern and western U.S. domains, respectively (Table 1). A similar
201 methodology is employed to identify continental U.S. extreme cold events by cataloguing 1-h
202 forecasts of 2-m temperature with grid points that featured temperatures less than their respective
203 1st-percentile temperatures. The identification scheme produces a total of 264 and 269 extreme
204 cold events during 1979–2014 within the eastern and western U.S. domains, respectively (Table
205 1). As previously mentioned, only ETEs that occurred during the cool season (Sep–May) will be
206 considered in this study (Table 1). It is left for future work to consider the subset of identified
207 ETEs that occurred during the summer (Jun–Aug).

208 Frequency distributions indicating where extreme warm events initiate within the eastern

and western U.S. domains during the cool season are shown in Fig. 2, along with the individual event centroids of every extreme warm event at the time of event initiation. The centroid for an individual extreme warm event at the time of event initiation is determined by calculating a weighted average of the latitude and longitude of every grid point that featured a temperature greater than its respective 99th-percentile temperature. Specifically, the latitude and longitude at every qualifying grid point is weighted by the magnitude of the difference between the temperature at the grid point and the 99th-percentile temperature for the grid point. Consequently, the event centroid is focused on those grid points where temperatures exceed their respective 99th-percentile temperatures by the largest margin.

A frequency maximum in eastern U.S. extreme warm event initiation is observed over the northern Plains with a secondary maximum extending from the central and southern Plains eastward towards the southern Mississippi River valley (Fig. 2a). Extreme warm events also initiate near the U.S. east coast, but at lower frequencies compared to locations farther west. In order to investigate differences between geographic regions with respect to the NPJ regimes that most frequently precede extreme warm event initiation, *k*-means clustering is used to classify the eastern U.S. extreme warm event centroids into three geographic clusters: the "Northern Plains", "Southern Plains", and "East Coast". The event centroids shown in Fig. 2a are colored based on their respective geographic cluster and match favorably with those locations that feature relative maxima in extreme warm event initiation. The frequency distribution for western U.S. extreme warm event initiation features two primary maxima located in the Pacific Northwest and in the northern U.S. Rocky Mountains, respectively (Fig. 2b). A secondary maximum in extreme warm event initiation is also observed over the southwestern U.S. As for eastern U.S. extreme warm events, *k*-means clustering is used to classify the western U.S. extreme warm event centroids into

three geographic clusters: the “Pacific Northwest”, “Northern Rockies”, and “Southwest”.

Spatial frequency distributions of extreme cold event initiation within the eastern and western U.S. domains during the cool season are shown in Fig. 3. Eastern U.S. extreme cold events most frequently initiate over the northern and southern Plains, with relative maxima also observed over the eastern Great Lakes, and the middle Mississippi River valley (Fig. 3a). In contrast to eastern U.S. extreme warm events, four geographic clusters were required in order to classify the extreme cold event centroids in a manner consistent with those locations that experience the highest frequency of extreme cold event initiation: the “Northern Plains”, “Southern Plains”, “Northeast”, and “Southeast”. For western U.S. extreme cold event initiation, a frequency maximum is observed over the northern U.S. Rocky Mountains, with a secondary maximum extending along the U.S. west coast and into southwest U.S. (Fig. 3b). As for western U.S. extreme warm events, the western U.S. extreme cold event centroids are classified into three geographic clusters: the “Pacific Northwest”, “Northern Rockies”, and “Southwest”.

b) The NPJ Phase Diagram

An effective way to examine the variability in synoptic-scale flow patterns that precede continental U.S. ETEs is through the development of an NPJ Phase Diagram that is constructed from the two leading modes of NPJ variability during the cool season. The following discussion is nearly identical to that in Winters et al. (2018) and is reproduced here given its relevance to this study. The NPJ Phase Diagram is developed by employing anomalies of the zonal component of the 250-hPa vector wind from the CFSR at every 6-h analysis time during 1979–2014 excluding the summer months. Anomalies are calculated as the deviation of the instantaneous 250-hPa zonal wind from a 21-day running mean centered on each analysis time in order to remove the 36-year mean as well as the annual and diurnal cycles. A traditional

empirical orthogonal function (EOF) analysis (Wilks 2011, Ch. 12) is subsequently performed on the 250-hPa zonal wind anomaly data within a horizontal domain bounded in latitude from 10°N to 80°N and in longitude from 100°E to 120°W in order to capture the North Pacific basin and to determine the two leading modes of NPJ variability.

The regression of 250-hPa zonal wind anomalies from the CFSR onto the two leading spatial patterns obtained from the traditional EOF analysis, EOF 1 and EOF 2, are illustrated in Fig. 4. EOF 1 explains 12.2% of the variance of 250-hPa zonal wind over the North Pacific and corresponds to longitudinal variability of 250-hPa zonal wind in the vicinity of the exit region of the climatological NPJ. A positive EOF 1 pattern (+EOF 1) is associated with a zonal extension of the exit region of the climatological NPJ (i.e., a jet extension), while a negative EOF 1 pattern (–EOF 1) is associated with a retraction of the exit region of the climatological NPJ (i.e., a jet retraction). EOF 2 explains 8.8% of the variance of 250-hPa zonal wind over the North Pacific and corresponds to latitudinal variability of 250-hPa zonal wind in the vicinity of the exit region of the climatological NPJ. A positive EOF 2 pattern (+EOF 2) is associated with a poleward shift of the exit region of the climatological NPJ (i.e., a poleward shift), while a negative EOF 2 pattern (–EOF 2) is associated with an equatorward shift of the exit region of the climatological NPJ (i.e., an equatorward shift). The EOF patterns and the combined variance explained by EOF 1 and EOF 2 are comparable to that found in previous studies of NPJ variability (Athanasiadis et al. 2010; Jaffe et al. 2011; Griffin and Martin 2017) and the two leading EOFs are statistically well separated using the methodology outlined in North et al. (1982).

250-hPa zonal wind anomalies at any particular analysis time can be regressed onto EOF 1 and EOF 2 to calculate the instantaneous principal components (PCs), PC 1 and PC 2, corresponding to that analysis time. The magnitude and sign of PC 1 and PC 2 are standardized

278 and provide an indication of how strongly the instantaneous 250-hPa zonal wind anomalies
279 project onto EOF 1 and EOF 2, respectively. Time series constructed from the instantaneous PCs
280 subsequently assist in characterizing the temporal evolution of the NPJ with respect to EOF 1
281 and EOF 2. The use of instantaneous PCs produces a noisy time series, however, due to the high-
282 frequency variability that characterizes the NPJ on daily time scales (e.g., Griffin and Martin
283 2017; their Fig. 1). Consequently, in an attempt to describe the evolution of the NPJ with greater
284 temporal coherence than the instantaneous PCs while preserving the high-frequency variability
285 of the NPJ on daily time scales, the instantaneous PCs are smoothed through the calculation of a
286 weighted average of the instantaneous PCs within ±24 h of each analysis time, t_0. The weight, w,
287 prescribed to the instantaneous PCs at each analysis time, t, within ±24 h of t_0 is defined as: $w =$
288 $5 - |t - t_0|/6$, for $|t - t_0| \leq 24$ h.

289 The weighted PCs at a particular analysis time can then be plotted on a two-dimensional
290 Cartesian grid (i.e., the NPJ Phase Diagram) in an effort to visualize the state of the NPJ and to
291 define the prevailing NPJ regime (Fig. 5). The position along the abscissa within the NPJ Phase
292 Diagram corresponds to the value of weighted PC 1 and indicates how strongly the 250-hPa
293 zonal wind anomalies project onto EOF 1. Positive values of weighted PC 1 represent a jet
294 extension and negative values represent a jet retraction. The position along the ordinate within
295 the NPJ Phase Diagram corresponds to the value of weighted PC 2 and indicates how strongly
296 the 250-hPa zonal wind anomalies project onto EOF 2. Positive values of weighted PC 2
297 represent a poleward shift of the exit region of the climatological NPJ and negative values
298 represent an equatorward shift.

299 As demonstrated in prior work, each NPJ regime strongly influences the character of the
300 downstream large-scale flow pattern over North America (e.g., Athanasiadis et al. 2010; Jaffe et

al. 2011; Griffin and Martin 2017; Winters et al. 2018). In an effort to illustrate this influence, the weighted PCs are calculated for all analysis times in the CFSR during 1979–2014 excluding the summer months and are subsequently classified into NPJ regimes according to Fig. 5. Following Winters et al. (2018), periods during which the NPJ is a distance of at least 1 PC unit from the origin of the NPJ Phase Diagram and characterized by the same NPJ regime for at least three consecutive days are isolated for composite analysis.

Composite analyses of the upper-tropospheric (Fig. 6) and lower-tropospheric (Fig. 7) flow patterns 4 days following the initiation of each NPJ regime highlight the characteristic large-scale flow patterns associated with each NPJ regime and demonstrate a relationship between each NPJ regime and the temperature distribution over North America. Specifically, the large-scale flow pattern favors below-normal temperatures over parts of eastern North America following jet extensions (Figs. 6a and 7a) and equatorward shifts (Figs. 6d and 7d), and above-normal temperatures following jet retractions (Figs. 6b and 7b) and poleward shifts (Figs. 6c and 7c). Over parts of western North America, below-normal temperatures are favored following jet retractions (Figs. 6b and 7b) and equatorward shifts (Fig. 6d and 7d), while above-normal temperatures are favored following jet extensions (Fig. 6a and 7a) and poleward shifts (Fig. 6c and 7c). Consequently, the composite analyses suggest that certain parts of North America may be more susceptible to the development of an ETE depending on the prevailing NPJ regime.

To examine the veracity of this suggestion, the prevailing NPJ regime prior to a continental U.S. ETE is determined by calculating the weighted PCs at 6-h intervals during the 3–7-day period prior to ETE initiation[2]. The weighted PCs are then averaged to determine the average position of the NPJ within the NPJ Phase Diagram 3–7 days prior ETE initiation (i.e.,

[2] The time of ETE initiation is rounded to the nearest analysis time for this investigation.

ETE PC 1, and ETE PC 2). Lastly, every ETE is classified into an NPJ regime based on the magnitude and sign of ETE PC 1 and ETE PC 2 according to Fig. 5.

3. NPJ regimes and NPJ evolutions conducive to cool season ETEs

a) Extreme warm events

The NPJ Phase Diagram and the NPJ regime classification scheme permit an identification of the NPJ regimes that frequently precede the initiation of continental U.S. ETEs during the cool season (Sep–May). Distributions of the average position of the NPJ within the NPJ Phase Diagram 3–7 days prior to the initiation of every eastern U.S. (Fig. 8a) and western U.S. (Fig. 9a) extreme warm event highlight the considerable variability that characterizes the upper-tropospheric flow pattern over the North Pacific prior to ETE initiation. Closer inspection, however, reveals several salient characteristics of continental U.S. extreme warm events. Eastern U.S. extreme warm events (N=239) are more common during the fall (Sep–Nov; N=86) and winter (Dec–Feb; N=84) compared to the spring (Mar–May; N=69), and most frequently initiate following jet retractions (N=69) and poleward shifts (N=66) throughout the cool season. These two NPJ regimes are consistent with those that generally favor above-normal temperatures over parts of eastern North America during nonextreme periods (Fig. 7). The most frequent NPJ regime prior to extreme warm event initiation varies based on the meteorological season, however. Specifically, extreme warm events most frequently initiate following equatorward shifts (N=26) during the fall, following jet retractions (N=27) during the winter, and following jet retractions (N=20) and poleward shifts (N=20) during the spring.

The characteristics of eastern U.S. extreme warm events vary considerably between the three eastern U.S. geographic clusters. Northern Plains extreme warm events (N=94) are most common during the winter (N=40) and are preceded by jet extensions (N=18) with the lowest

346 frequency throughout the cool season (Fig. 8b). However, those Northern Plains events that
347 occur during the winter are nearly as frequent following jet extensions (N=12) as they are
348 following jet retractions (N=11) and poleward shifts (N=10). Similar to Northern Plains extreme
349 warm events, Southern Plains events (N=84) are also more common during the winter (N=33)
350 compared to fall (N=26) and spring (N=25). Southern Plains events most frequently initiate
351 following jet retractions (N=35) throughout the cool season and do not exhibit any seasonal
352 variability with respect to the most frequent NPJ regime prior to ETE initiation (Fig. 8c). In
353 contrast to Northern Plains and Southern Plains extreme warm events, East Coast events (N=61)
354 are more common during the fall (N=31) and spring (N=19) compared to the winter (N=11). East
355 Coast events most frequently initiate following poleward shifts (N=20) and equatorward shifts
356 (N=17) throughout the cool season, though the most frequent NPJ regime prior to ETE initiation
357 varies based on the meteorological season (Fig. 8d).

358 Western U.S. extreme warm events (N=204) are most common during the winter (N=81)
359 and are preceded by jet retractions (N=41) with the lowest frequency throughout the cool season
360 (Fig. 9a). This result is consistent with the observation that a jet retraction is the only NPJ regime
361 that favors below-normal temperatures over the western U.S. during nonextreme periods (Fig.
362 7b). Similar to eastern U.S. extreme warm events, the most frequent NPJ regimes that precede
363 the initiation of western U.S. events vary based on the meteorological season. Specifically,
364 western U.S. extreme warm events most frequently initiate following poleward shifts (N=23) and
365 jet retractions (N=19) during the fall, following jet extensions (N=32) and equatorward shifts
366 (N=25) during the winter, and following equatorward shifts (N=20) and poleward shifts (N=18)
367 during the spring.

368 Consideration of events within each of the three western U.S. geographic clusters adds

insight into the characteristics of western U.S. extreme warm events. Pacific Northwest extreme warm events (N=89) are most common during the winter (N=37), and most frequently initiate following jet extensions (N=27) and equatorward shifts (N=27) throughout the cool season (Fig. 9b). As observed for all western U.S. extreme warm events, however, the most frequent NPJ regimes prior to Pacific Northwest events vary based on the meteorological season. Specifically, Pacific Northwest extreme warm events most frequently initiate following poleward shifts (N=11) and jet retractions (N=7) during the fall, and following jet extensions and equatorward shifts during the winter (N=16 and N=13, respectively) and spring (N=8 and N=10, respectively) (Fig. 9b). The most frequent NPJ regime prior to Northern Rockies extreme warm events (N=46) is also characterized by considerable seasonal variability (Fig. 9c). However, in contrast to Pacific Northwest extreme warm events, Northern Rockies events initiate following equatorward shifts (N=7) with the lowest frequency throughout the cool season. Southwest extreme warm events (N=69) initiate most frequently following equatorward shifts (N=20) and poleward shifts (N=19) throughout the cool season, though the most frequent NPJ regime prior to ETE initiation differs based on the meteorological season in this region, as well (Fig. 9d).

The construction of composite trajectories of the NPJ within the NPJ Phase Diagram provides an objective characterization of the evolution of the NPJ during the 10-day period prior to ETE initiation. Composite trajectories of the NPJ within the NPJ Phase Diagram are constructed by calculating the weighted PCs at 6-h intervals during a 10-day period prior to the initiation of every ETE. The weighted PCs prior to each individual ETE are then shifted so that the position of the NPJ 10 days prior to ETE initiation always lies at the origin of the NPJ Phase Diagram. Lastly, the weighted PCs that correspond to the same lead time prior to ETE initiation are averaged among all ETEs within the same geographic cluster to construct a composite

392 trajectory.

393 The composite trajectories of the NPJ within the NPJ Phase Diagram prior to all eastern
394 U.S. extreme warm events and events within the three eastern U.S. geographic clusters are
395 shown in Fig. 10a. Consistent with the observation that eastern U.S. extreme warm events most
396 frequently initiate following jet retractions and poleward shifts throughout the cool season (Fig.
397 8a), the composite trajectory for all eastern U.S. events indicates that the NPJ evolves towards a
398 jet retraction and poleward shift during the 10-day period prior to ETE initiation. The same result
399 is generally found for events within each of the eastern U.S. geographic clusters as well, with
400 Northern Plains events characterized by an NPJ that evolves towards a poleward shift, and
401 Southern Plains and East Coast events characterized by an NPJ that evolves towards a jet
402 retraction.

403 The composite trajectories prior to all western U.S. extreme warm events and events
404 within the three western U.S. geographic clusters exhibit considerable differences compared to
405 the trajectories for eastern U.S. events (Fig. 10b). In particular, the composite trajectory for all
406 western U.S. extreme warm events indicates that the NPJ evolves towards a jet extension and
407 equatorward shift during the 10-day period prior to ETE initiation, rather than the jet retraction
408 and poleward shift observed for all eastern U.S. events (Fig. 10a). A comparison between
409 trajectories for the three western U.S. geographic clusters demonstrates that Pacific Northwest
410 events are characterized by an NPJ that evolves considerably towards a jet extension during the
411 10-day period prior to ETE initiation while Southwest events are characterized by an NPJ that
412 evolves considerably towards an equatorward shift and jet retraction prior to ETE initiation. In
413 comparison to the composite trajectories associated with Pacific Northwest and Southwest
414 events, the trajectory for Northern Rockies events does not deviate far from the origin of the NPJ

Phase Diagram. Consequently, Northern Rockies events do not appear to have a preferred NPJ evolution prior to initiation.

b) Extreme cold events

The variability in NPJ regimes that precede continental U.S. extreme cold events is also examined in the context of the NPJ Phase Diagram. Figure 11a indicates that eastern U.S. extreme cold events (N=173) are more common during the winter (N=63) and spring (N=60) compared to the fall (N=50), and most frequently initiate following equatorward shifts (N=73) by a large margin throughout the cool season. This result is consistent with the observation that equatorward shifts generally favor the development of below-normal temperatures across northern North America during nonextreme periods (Fig. 7d). The most frequent NPJ regime prior to extreme cold event initiation does vary based on meteorological season, however. In particular, extreme cold events most frequently initiate following both equatorward shifts (N=17) and jet extensions (N=17) during the fall, and following only equatorward shifts during the winter (N=30) and spring (N=26). Additionally, while eastern U.S. extreme cold events are not as frequent following jet retractions (N=30) throughout the cool season as they are following equatorward shifts (N=73) and jet extensions (N=47), it is notable that half of the extreme cold events that initiate following jet retractions occur during the spring (N=15).

The same characteristics derived for all eastern U.S. extreme cold events generally apply to each of the four eastern U.S. geographic clusters. Specifically, extreme cold events within each geographic cluster are most common during both the winter and/or spring, and most frequently initiate following equatorward shifts throughout the cool season (Figs. 11b–e). The lack of any considerable differences in extreme cold event characteristics between the four eastern U.S. geographic clusters stands in contrast to the considerable differences observed

between geographic clusters for eastern U.S. extreme warm events (Figs. 8a–d). Consequently, this result demonstrates that there is larger variability among the upper-tropospheric flow patterns that are conducive to the development of eastern U.S. extreme warm events than among those that are conducive to eastern U.S. extreme cold events.

In contrast to western U.S. extreme warm events (Fig. 9a), western U.S. extreme cold events (N=196) are the least common during the winter (N=52) and are most common during the spring (N=83) (Fig. 12a). Similar distributions based on meteorological season are also observed for events within each of the three western U.S. geographic clusters (Figs. 12b–d). Additionally, western U.S. extreme cold events most frequently initiate following jet retractions (N=59) throughout the cool season (Fig. 12a), rather than with the lowest frequency as observed for extreme warm events (Fig. 9a). This result aligns with the observation that jet retractions generally favor below-normal temperatures along the U.S. west coast during nonextreme periods (Fig. 7b). As observed for other categories of ETEs, the most frequent NPJ regime prior to the initiation of western U.S. extreme cold events varies based on meteorological season. Specifically, extreme cold events most frequently initiate following equatorward shifts (N=21) and jet extensions (N=18) during the fall, and following jet retractions during the winter (N=21) and spring (N=28).

The western U.S. geographic clusters, unlike the eastern U.S. geographic clusters, differ considerably with respect to the NPJ regime that most frequently precedes extreme cold event initiation. Pacific Northwest events (N=78) most frequently initiate following jet retractions (N=31) throughout the cool season (Fig. 12b), with most of those events occurring during the winter (N=11) and spring (N=15). During the fall, however, Pacific Northwest extreme cold events initiate following equatorward shifts (N=12) more frequently than the other NPJ regimes.

461 Northern Rockies extreme cold events, on the other hand, most frequently initiate following
462 equatorward shifts (N=22) throughout the cool season (Fig. 12c), while Southwest events initiate
463 following equatorward shifts (N=10) with the *lowest* frequency throughout the cool season (Fig.
464 12d). The most frequent NPJ regime prior to the initiation of Southwest events varies based on
465 meteorological season, with events most frequently initiating following jet extensions during the
466 fall (N=8), following jet retractions during the winter (N=6), and nearly equivalently following
467 jet extensions (N=9), jet retractions (N=8), and poleward shifts (N=8) during the spring.

468 In contrast to the composite trajectories for continental U.S. extreme warm events (Fig.
469 10), the composite trajectories for continental U.S. extreme cold events are rather similar
470 between the eastern and western U.S. domains (Figs. 13a,b). In particular, the composite
471 trajectory for all eastern U.S. extreme cold events indicates that the NPJ evolves towards an
472 equatorward shift and jet extension during the 10-day period prior to event initiation (Fig. 13a),
473 consistent with those NPJ regimes that most frequently precede the initiation of eastern U.S.
474 extreme cold events throughout the cool season (Fig. 11a). Composite trajectories for events
475 within the Northern Plains, Southern Plains, and Southeast clusters also suggest that the NPJ
476 generally evolves towards an equatorward shift during the 10-day period prior to event initiation.
477 The composite trajectory for events within the Northeast cluster is somewhat of an outlier,
478 however, with the NPJ evolving towards a jet extension during the 10-day period prior to event
479 initiation.

480 The composite trajectory for all western U.S. extreme cold events indicates that the NPJ
481 evolves towards an equatorward shift and a slight jet extension during the 10-day period prior to
482 event initiation (Fig. 13b). The Pacific Northwest and Northern Rockies composite trajectories
483 are comparable to the trajectory for all western U.S. events in that they both show the NPJ

484 evolving towards an equatorward shift and jet extension by the time of event initiation. The
485 Southwest composite trajectory also suggests that the NPJ evolves towards an equatorward shift,
486 but the trajectory is different compared to the Pacific Northwest and Northern Rockies
487 trajectories given that the NPJ evolves towards a jet retraction by the time of event initiation
488 rather than a jet extension.

489 **4. Composite evolution of Southern Plains extreme warm events preceded by a jet**
490 **retraction**

491 The utility of the NPJ Phase Diagram is that it can be used to isolate ETEs within a
492 particular geographic region that initiate following the same NPJ regime. A composite analysis
493 can subsequently be performed on ETEs that are preceded by the same NPJ regime in order to
494 further investigate the types of synoptic-scale flow evolutions that are conducive to ETE
495 initiation within that geographic region. The forthcoming discussion provides an illustrative
496 example that showcases the utility of such an analysis by considering the synoptic-scale flow
497 evolution most conducive to Southern Plains extreme warm events. The Southern Plains cluster
498 is selected for analysis given that it is the only geographic region where the most frequent NPJ
499 regime prior to both extreme warm and cold events does not vary based on the meteorological
500 season (Figs. 8, 9, 11 and 12). Furthermore, extreme warm events are selected due to the limited
501 consideration those events have received in the refereed literature compared to extreme cold
502 events.

503 A composite analysis of the synoptic-scale flow evolution observed to be most conducive
504 to the initiation of Southern Plains extreme warm events during the cool season is performed by
505 isolating those Southern Plains extreme warm events that are characterized by a jet retraction
506 prior to event initiation (N=35; Fig. 8c). The latitude and longitude of the individual Southern

507 Plains event centroids (Fig. 2a) are then averaged to determine the position of a composite
508 centroid. The composite analyses are constructed by, first, shifting the CFSR data for each
509 individual event so that each individual event centroid matches the position of the composite
510 centroid and, second, by averaging the shifted CFSR data at each grid point across all cases
511 within the horizontal domain shown in Fig. 14. A two-sided Student's *t* test is performed on the
512 composite 250-hPa geopotential height anomalies and 850-hPa temperature anomalies to identify
513 regions that are statistically significantly different from climatology at the 99% confidence level.
514 The composite evolution of the synoptic-scale flow pattern during the 6-day period prior
515 to event initiation is provided in Fig. 14 and is comparable to the evolution of southeast U.S.
516 extreme warm events that develop during a negative phase of the PNA discussed by Westby and
517 Black (2015). An anomalous upper-tropospheric ridge is located over the central North Pacific 6
518 days prior to event initiation, resulting in a jet retraction over the western North Pacific and a
519 split NPJ to the east of the dateline (Fig. 14a). Farther downstream, an anomalous upper-
520 tropospheric ridge is collocated with above-normal 850-hPa temperatures over the southern
521 Plains and northern Mexico (Fig. 14b), suggesting that the synoptic-scale environment may be
522 preconditioned for the development of extreme warmth in that location.
523 4 days prior to event initiation, the anomalous North Pacific ridge amplifies further
524 compared to the prior time in conjunction with surface cyclogenesis beneath the left-exit region
525 of the retracted NPJ (Figs. 14c,d). Specifically, the surface cyclone facilitates anomalous warm-
526 air advection over the central North Pacific that contributes to both upper-tropospheric height
527 rises and forcing for quasigeostrophic ascent (not shown). The presence of anomalous
528 precipitable water in the central North Pacific also suggests that condensational heating is likely
529 associated with any areas of ascent and, consequently, that diabatic processes contribute to the

observed ridge amplification (e.g., Massacand et al. 2001; Riemer et al. 2008; Torn 2010; Grams et al. 2011; Madonna et al. 2014; Pfahl et al. 2015; Torn and Hakim 2015; Grams and Archambault 2016; Bosart et al. 2017). Central North Pacific ridge amplification subsequently results in the amplification of the downstream upper-tropospheric flow pattern 2 days prior to event initiation (Fig. 14e), including the development of a positively-tilted trough along the west coast of North America and additional ridge amplification over the southern Plains. The amplified upper-tropospheric flow pattern also supports lee cyclogenesis over the northern U.S. Rocky Mountains and surface anticyclogenesis over the southeast U.S. (Fig. 14f). The intensified pressure gradient between the lee cyclone and surface anticyclone induces southwesterly geostrophic flow over central North America and the concomitant advection of anomalous warmth from northern Mexico into the southern Plains.

The lee cyclone intensifies further by the time of event initiation beneath the entrance region of a 250-hPa jet streak and in conjunction with continued amplification of the upper-tropospheric flow pattern (Figs. 14g,h). The intensified lee cyclone subsequently facilitates stronger southwesterly geostrophic flow over the southern Plains than at the prior time, which ensures that the advection of anomalous warmth into the southern Plains continues unabated until the time of event initiation. Notably, the composite evolution also features anomalous precipitable water over the middle Mississippi River valley at the time of event initiation (Fig. 14g). Given the strong dynamical forcing for ascent provided by the amplified upper-tropospheric flow pattern and the presence of the lee cyclone, the evolution of a Southern Plains extreme warm event bears a strong resemblance to synoptic-scale flow evolutions that are conducive to the development of eastern U.S. extreme precipitation events during the cool season (e.g., Moore et al. 2015; Moore 2017). Consequently, it is possible that heavy

553 precipitation events may accompany the development of Southern Plains extreme warm events
554 on occasion.

555 **5. Discussion**

556 The utility of the NPJ Phase Diagram is that it provides a common framework for
557 examining the antecedent synoptic-scale flow patterns associated with ETEs regardless of the
558 location of the ETE within the continental U.S. Overall, eastern U.S. extreme warm events are
559 most frequent following jet retractions and poleward shifts and are characterized by an NPJ that
560 evolves towards those same two NPJ regimes within the NPJ Phase Diagram during the 10-day
561 period prior to ETE initiation. Western U.S. extreme warm events, however, are the *least*
562 frequent following jet retractions and are characterized by an NPJ that evolves towards a jet
563 extension and equatorward shift within the NPJ Phase Diagram during the 10-day period prior to
564 ETE initiation. Eastern U.S. extreme cold events are most frequent following equatorward shifts
565 by a large margin, while western U.S. extreme cold events are most frequent following both jet
566 retractions and equatorward shifts. Furthermore, both eastern and western U.S. extreme cold
567 events are generally characterized by an evolution of the NPJ towards an equatorward shift
568 during the 10-day period prior to ETE initiation. Therefore, the results demonstrate that
569 knowledge of both the prevailing NPJ regime and the NPJ evolution indicates the degree to
570 which the synoptic-scale flow pattern may be conducive to ETE initiation within certain parts of
571 the continental U.S.

572 While the NPJ regimes and NPJ evolutions described above are those that most
573 frequently precede all eastern and western U.S. ETEs throughout the cool season, the most
574 frequent NPJ regime prior to ETE initiation varies considerably based on the specific location of
575 ETE initiation within the eastern and western U.S. domains as well as the meteorological season.

As an example, Pacific Northwest extreme cold events most frequently initiate following jet retractions throughout the cool season, while Northern Rockies extreme cold events initiate following jet retractions with the *lowest* frequency throughout the cool season. Additionally, Pacific Northwest extreme cold events most frequently initiate following jet retractions during only the winter and spring. During the fall, Pacific Northwest events most frequently initiate following equatorward shifts. The geographic and seasonal variability of NPJ regimes that are most conducive to ETE initiation motivates future investigations to examine ETE initiation within focused geographic regions, similar to the approaches of Westby and Black (2015), Grotjahn et al. (2017), and Xie et al. (2017).

The NPJ Phase Diagram and the results from the present study can be leveraged to perform these geographically-focused investigations. As an illustrative example, the analysis in section 4 employed the NPJ Phase Diagram to examine the synoptic-scale flow evolution that is most conducive to the initiation of Southern Plains extreme warm events in greater detail. In geographic clusters where multiple NPJ regimes are most frequent prior to ETE initiation (e.g., Pacific Northwest extreme warm events), or where the most frequent NPJ regime varies based on meteorological season (e.g., Pacific Northwest extreme cold events), the NPJ Phase Diagram can be applied to isolate ETEs that are preceded by the same NPJ regime. Composite analyses can then be performed on events that are preceded by the same NPJ regime in order to examine the differences between synoptic-scale flow evolutions that are equally conducive to the initiation of ETEs. Such examinations represent promising areas of future work.

The capability of the NPJ Phase Diagram to identify NPJ regimes and NPJ evolutions that are conducive to the development of ETEs highlights the potential for the NPJ Phase Diagram to add value to operational medium-range (6–10 day) forecasts of temperature over the

599 continental U.S. In particular, the NPJ Phase Diagram can be employed operationally to
600 determine the prevailing NPJ regime and the forecast evolution of the NPJ. This information can
601 be paired with the results of this study to determine geographic locations that may be more
602 susceptible to the development of anomalous temperatures during the medium-range period.
603 Despite this potential, however, additional work utilizing the NPJ Phase Diagram is required in
604 order to differentiate between synoptic-scale flow evolutions that are conducive to ETEs versus
605 those that result in nonextreme events. Additionally, Winters et al. (2018) indicate that certain
606 NPJ regimes are generally characterized by enhanced or reduced forecast skill during the
607 medium-range forecast period. Future work examining the medium-range forecast skill of ETEs
608 with respect to the NPJ Phase Diagram might reveal whether certain synoptic-scale flow
609 evolutions prior to ETEs are characterized by enhanced or reduced forecast skill.
610 Lastly, the NPJ Phase Diagram can be applied to examine the variability in NPJ regimes
611 that precede other types of North American EWEs during the cool season. For instance, the NPJ
612 Phase Diagram can be applied to determine the NPJ regimes that are conducive to the
613 development of extreme precipitation events (e.g., Moore et al. 2015; Moore 2017), landfalling
614 atmospheric river events (e.g., Zhu and Newell 1998; Ralph et al. 2004; Neiman et al. 2008;
615 Cordeira et al. 2013; Mundhenk et al. 2016; Gershunov et al. 2017), severe weather outbreaks
616 (e.g., Cook and Schaefer 2008; Allen et al. 2015; Tippett et al. 2015; Gensini and Marinaro
617 2016; Cook et al. 2017), and rapidly-deepening midlatitude cyclones (e.g., Sanders and Gyakum
618 1980; Bosart et al. 1996; Isard et al. 2000; Grise et al. 2013; Bentley 2018). As demonstrated for
619 ETEs, these examinations have the potential to add value to operational forecasts of EWEs
620 through further understanding of the environments that are conducive to EWE development.
621

Acknowledgments

The authors thank Mike Bodner, Daniel Halperin, Arlene Laing, Bill Lamberson, Sara Ganetis, and Josh Kastman for their constructive discussions concerning the NPJ Phase Diagram. The authors also thank the National Oceanic and Atmospheric Administration for its support of this work via Grant NA15NWS4680006.

645 **References**
646
647 Allen, J. T., M. K. Tippett, and A. H. Sobel, 2015: Influence of the El Niño/Southern Oscillation
648 on tornado and hail frequency in the United States. *Nat. Geosci.*, **8,** 278–283, doi:
649 10.1038/ngeo2385.
650 Athanasiadis, P. J., J. M. Wallace, and J. J. Wettstein, 2010: Patterns of wintertime jet stream
651 variability and their relation to the storm tracks. *J. Atmos. Sci.*, **67**, 1361–1381, doi:
652 10.1175/2009JAS3270.1.
653 Bell, G. D., and L. F. Bosart, 1988: Appalachian cold-air damming. *Mon. Wea. Rev*., **116,** 137–
654 161, doi: 10.1175/1520-0493(1988)116<0137:ACAD>2.0.CO;2.
655 Bentley, A. M., 2018: Extratropical cyclones leading to extreme weather events over central and
656 eastern North America. Ph.D. Dissertation, University at Albany–SUNY, 158 pp.
657 Bosart, L. F., G. J. Hakim, K. R. Tyle, M. A. Bedrick, W. E. Bracken, M. J. Dickinson, and D.
658 M. Schultz, 1996: Large-scale antecedent conditions associated with the 12–14 March
659 1993 cyclone ("Superstorm '93") over eastern North America. *Mon. Wea. Rev,*, **124,**
660 1865–1891, doi: 10.1175/1520-0493(1996)124<1865:LSACAW>2.0.CO;2.
661 Bosart, L. F., B. J. Moore, J. M. Cordeira, and H. M. Archambault, 2017: Interactions of North
662 Pacific tropical, midlatitude, and polar disturbances resulting in linked extreme weather
663 events over North America in October 2007. *Mon. Wea. Rev.*, **145,** 1245–1273, doi:
664 10.1175/MWR-D-16-0230.1.
665 Brewer, M. C., C. F. Mass, and B. E. Potter, 2012: The west coast thermal trough: Climatology
666 and synoptic evolution. *Mon. Wea. Rev.*, **140,** 3820–3843, doi: 10.1175/MWR-D-12-
667 00078.1.

668 Brewer, M. C., C. F. Mass, and B. E. Potter, 2012: The west coast thermal trough: Mesoscale
669 evolution and sensitivity to terrain and surface fluxes. *Mon. Wea. Rev.*, **141,** 2869–2896,
670 doi: 10.1175/MWR-D-12-00305.1.
671 Carrera, M. L., R. W. Higgins, and V. E. Kousky, 2004: Downstream weather impacts associated
672 with atmospheric blocking over the northeast Pacific. *J. Climate*, **17,** 4823–4839, doi:
673 10.1175/JCLI-3237.1.
674 Cellitti, M. P., J. E. Walsh, R. M. Rauber, and D. H. Portis, 2016: Extreme cold air outbreaks
675 over the United States, the polar vortex, and the large-scale circulation. *J. Geophys. Res.*,
676 **111,** D02114, doi: 10.1029/2005JD006273.
677 Colle, B. A., and C. F. Mass, 1995: The structure and evolution of cold surges east of the Rocky
678 Mountains. *Mon. Wea. Rev.*, **123,** 2577–2610, doi: 10.1175/1520-
679 0493(1995)123<2577:TSAEOC>2.0.CO;2.
680 Colucci, S. J., and J. C. Davenport, 1987: Rapid surface anticyclogenesis: Synoptic climatology
681 and attendant large-scale circulation changes. *Mon. Wea. Rev.*, **115,** 822–836, doi:
682 10.1175/1520-0493(1987)115<0822:RSASCA>2.0.CO;2.
683 Cook, A. R., and J. T. Schaefer, 2008: The relation of El Niño–Southern Oscillation (ENSO) to
684 winter tornado outbreaks. *Mon. Wea. Rev.*, **136,** 3121–3137, doi:
685 10.1175/2007MWR2171.1.
686 Cook, A. R., L. M. Leslie, D. B. Parsons, and J. T. Schaefer, 2017: The impact of El Niño–
687 Southern Oscillation (ENSO) on winter and early spring U.S. tornado outbreaks. *J. Appl.*
688 *Meteor. Climatol.*, **56,** 2455–2478, doi: 10.1175/JAMC-D-16-0249.1.

689 Cordeira, J. M., and L. F. Bosart, 2010: The antecedent large-scale conditions of the "Perfect
690 Storms" of late October and early November 1991. *Mon. Wea. Rev.*, **138,** 2546–2569,
691 doi: 10.1175/2010MWR3280.1.
692 Cordeira, J. M., F. M. Ralph, and B. J. Moore, 2013: The development and evolution of two
693 atmospheric rivers in proximity to western North Pacific tropical cyclones in October
694 2010. *Mon. Wea. Rev.*, **141,** 4234–4255, doi: 10.1175/MWR-D-13-00019.1.
695 Dallavalle, J. P., and L. F. Bosart, 1975: A synoptic investigation of anticyclogenesis
696 accompanying North American polar air outbreaks. *Mon. Wea. Rev.*, **103,** 941–957, doi:
697 10.1175/1520-0493(1975)103<0941:ASIOAA>2.0.CO;2.
698 Dole, R., M. Hoerling, A. Kumar, J. Eischeid, J. Perlwitz, X.-W. Quan, G. Kiladis, R. Webb, D.
699 Murray, M. Chen, K. Wolter, and T. Zhang, 2014: The making of an extreme event:
700 Putting the pieces together. *Bull. Amer. Meteor. Soc.*, **95,** 427–440, doi: 10.1175/BAMS-
701 D-12-00069.1.
702 Downton, M. W., and K. A. Miller, 1993: The freeze risk to Florida citrus. Part II: Temperature
703 variability and circulation patterns. *J. Climate*, **6,** 364–372, doi: 10.1175/1520-
704 0442(1993)006<0364:TFRTFC>2.0.CO;2.
705 Gensini, V. A., and A. Marinaro, 2016: Tornado frequency in the United States related to global
706 relative angular momentum. *Mon. Wea. Rev.*, **144,** 801–810, doi: 10.1175/MWR-D-15-
707 0289.1.
708 Gershunov, A., T. Shulgina, F. M. Ralph, D. A. Lavers, and J. J. Rutz, 2017: Assessing the
709 climate-scale variability of atmospheric rivers affecting western North America.
710 *Geophys. Res. Lett.*, **44,** 7900–7908, doi: 10.1002/2017GL074175.

711 Grams, C. M., and Coauthors, 2011: The key role of diabatic processes in modifying the upper-
712 tropospheric wave guide: A North Atlantic case-study. *Quart. J. Roy. Meteor. Soc.*, **137,**
713 2174–2193, doi: 10.1002/qj.891.
714 Grams, C. M., and H. M. Archambault, 2016: The key role of diabatic outflow in amplifying the
715 midlatitude flow: A representative case study of weather systems surrounding western
716 North Pacific extratropical transition. *Mon. Wea. Rev.*, **144**, 3847–3869, doi:
717 10.1175/MWR-D-15-0419.1.
718 Griffin, K. S., and J. E. Martin, 2017: Synoptic features associated with temporally coherent
719 modes of variability of the North Pacific jet stream. *J. Climate*, **30**, 39–54, doi:
720 10.1175/JCLI-D-15-0833.1.
721 Grise, K. M., S.-W. Son, J. R. Gyakum, 2013: Intraseasonal and interannual variability in North
722 American storm tracks and its relationship to equatorial Pacific variability. *Mon. Wea.*
723 *Rev.*, **141,** 3610–3625, doi: 10.1175/MWR-D-12-00322.1.
724 Grotjahn, R., and Coauthors, 2016: North American extreme temperature events and related
725 large scale meteorological patterns: A review of statistical methods, dynamics, modeling,
726 and trends. *Climate Dyn.*, **46,** 1151–1184, doi: 10.1007/s00382-015-2638-6.
727 Grotjahn, R., and R. Zhang, 2017: Synoptic analysis of cold air outbreaks over the California
728 Central Valley. *J. Climate*, **30,** 9417–9433, doi: 10.1175/JCLI-D-17-0167.1.
729 Gu, L., P. J. Hanson, W. Mac Post, D. P. Kaiser, B. Yang, R. Nemani, S. G. Pallardy, and T.
730 Meyers, 2008: The 2007 eastern US spring freeze: Increased cold damage in a warming
731 world? *Bioscience*, **58,** 253–262, doi: 10.1641/B580311.

732 Guirguis, K., A. Gershunov, R. Schwartz, S. Bennett, 2011: Recent warm and cold daily winter
733 temperature extremes in the Northern Hemisphere. *Geophys. Res. Lett.*, **38,** L17701, doi:
734 10.1029/2011GL048762.
735 Hartjenstein, G., and R. Bleck, 1991: Factors affecting cold-air outbreaks east of the Rocky
736 Mountains. *Mon. Wea. Rev.*, **119,** 2280–2292, doi: 10.1175/1520-
737 0493(1991)119<2280:FACAOE>2.0.CO;2.
738 Hartmann, D. L., 2015: Pacific sea surface temperature and the winter of 2014. *Geophys. Res.*
739 *Lett.*, **42,** 1894–1902, doi: 10.1002/2015GL063083.
740 Higgins, R. W., A. Leetmaa, and V. E. Kousky, 2002: Relationships between climate variability
741 and winter temperature extremes in the United States. *J. Climate*, **15,** 1555–1572, doi:
742 10.1175/1520-0442(2002)015<1555:RBCVAW>2.0.CO;2.
743 Hoerling, M., A. Kumar, R. Dole, J. W. Nielsen-Gammon, J. Eischeid, J. Perlwitz, X.-W. Quan,
744 T. Zhang, P. Pegion, and M. Chen, 2013: Anatomy of an extreme event. *J. Climate*, **26,**
745 2811–2832, doi: 10.1175/JCLI-D-12-00270.1.
746 Isard, S. A., J. R. Angel, and G. T. VanDyke, 2000: Zones of origin for Great Lakes cyclones in
747 North America, 1899–1996. *Mon. Wea. Rev.*, **128,** 474–485, doi: 10.1175/1520-
748 0493(2000)128<0474:ZOOFGL>2.0.CO;2.
749 Jaffe, S. C., J. E. Martin, D. J. Vimont, and D. J. Lorenz, 2011: A synoptic climatology of
750 episodic, subseasonal retractions of the Pacific jet. *J. Climate*, **24**, 2846–2860, doi:
751 10.1175/2010JCLI3995.1.
752 Kenyon, J., and G. C. Hegerl, 2008: Influence of modes of climate variability on global
753 temperature extremes. *J. Climate*, **21,** 3872–3889, doi: 10.1175/2008JCLI2125.1.

754 Konrad, C. E., II, 1996: Relationships between the intensity of cold-air outbreaks and the
755 evolution of synoptic and planetary-scale features over North America. *Mon. Wea. Rev.*,
756 **124,** 1067–1083, doi: 10.1175/1520-0493(1996)124<1067:RBTIOC>2.0.CO;2.
757 Konrad, C. E., II, and S. J. Colucci, 1989: An examination of extreme cold air outbreaks over
758 eastern North America. *Mon. Wea. Rev.*, **117,** 2687–2700, doi: 10.1175/1520-
759 0493(1989)117<2687:AEOECA>2.0.CO;2.
760 Lim, Y.-K., and S. D. Schubert, 2011: The impact of ENSO and the Arctic Oscillation on winter
761 temperature extremes in the southeast United States. *Geophys. Res. Lett.*, **38,** L15706,
762 doi: 10.1029/2011GL048283.
763 Loikith, P. C., and A. J. Broccoli, 2012: Characteristics of observed atmospheric circulation
764 patterns associated with temperature extremes over North America. *J. Climate*, **25,** 7266–
765 7281, doi: 10.1175/JCLI-D-11-00709.1.
766 Loikith, P. C., and A. J. Broccoli, 2014: The influence of recurrent modes of climate variability
767 on the occurrence of winter and summer extreme temperatures over North America. *J.*
768 *Climate*, **27,** 1600–1618, doi: 10.1175/JCLI-D-13-00068.1.
769 Loikith, P. C., B. R. Lintner, and A. Sweeney, 2017: Characterizing large-scale meteorological
770 patterns and associated temperature and precipitation extremes over the northwestern
771 United States using self-organizing maps. *J. Climate*, **30,** 2829–2847, doi: 10.1175/JCLI-
772 D-16-0670.1.
773 Madonna, E., H. Wernli, H. Joos, and O. Martius, 2014: Warm conveyor belts in the ERA-
774 Interim dataset (1979–2010). Part I: Climatology and potential vorticity evolution. *J.*
775 *Climate*, **27,** 3–26, doi: 10.1175/JCLI-D-12-00720.1.

776 Massacand, A. C., H. Wernli, and H. C. Davies, 2001: Influence of upstream diabatic heating
777 upon an alpine event of heavy precipitation. *Mon. Wea. Rev.*, **129**, 2822–2828, doi:
778 10.1175/1520-0493(2001)129<2822:IOUDHU>2.0.CO;2.
779 Meehl, G. A., C. Tebaldi, 2004: More intense, more frequent, and longer lasting heat waves in
780 the 21st century. *Science*, **305,** 994–997, doi: 10.1126/science.1098704.
781 Meehl, G. A., C. Tebaldi, H. Teng, and T. C. Peterson, 2007: Current and future U.S. weather
782 extremes and El Niño. *Geophys. Res. Lett.*, **34,** L20704, doi: 10.1029/2007GL031027.
783 Moore, B. J., 2017: Rossby wave breaking and widespread extreme precipitation events in the
784 central and eastern U.S. Ph.D. Dissertation, University at Albany–SUNY, 188 pp.
785 Moore, B. J., K. M. Mahoney, E. M. Sukovich, R. Cifelli, and T. M. Hamill, 2015: Climatology
786 and environmental characteristics of extreme precipitation events in the southeastern
787 United States. *Mon. Wea. Rev.*, **143,** 718–741, doi: 10.1175/MWR-D-14-00065.1.
788 Mundhenk, B. D., E. A. Barnes, and E. D. Maloney, 2016: All-season climatology and
789 variability of atmospheric river frequencies over the North Pacific. *J. Climate*, **29,** 4885–
790 4903, doi: 10.1175/JCLI-D-15-0655.1.
791 Neiman, P. J., F. M. Ralph, G. A. Wick, J. D. Lundquist, and M. D. Dettinger, 2008:
792 Meteorological characteristics and overland precipitation impacts of atmospheric rivers
793 affecting the west coast of North America based on eight years of SSM/I satellite
794 observations. *J. Hydrometeor.*, **9,** 22–47, doi: 10.1175/2007JHM855.1.
795 North, G. R., T. L. Bell, R. F. Cahalan, and F. J. Moeng, 1982: Sampling errors in the estimation
796 of empirical orthogonal functions. *Mon. Wea. Rev.*, **110**, 699–706, doi: 10.1175/1520-
797 0493(1982)110<0699:SEITEO>2.0.CO;2.

798 Peterson, T. C., M. P. Hoerling, P. A. Stott, and S. C. Herring, 2013: Explaining extreme events
799 of 2012 from a climate perspective. *Bull. Amer. Meteor. Soc.*, **94,** S1–S74, doi:
800 10.1175/BAMS-D-13-00085.1.
801 Peterson, A. G., and J. T. Abatzoglou, 2014: Observed changes in false springs over the
802 contiguous United States. *Geophys. Res. Lett.*, **41,** 2156–2162, doi:
803 10.1002/2014GL059266.
804 Pfahl, S., C. Schwierz, M. Croci-Maspoli, C. M. Grams, and H. Wernli, 2015: Importance of
805 latent heat release in ascending air streams for atmospheric blocking. *Nat. Geosci.*, **8**,
806 610–614, doi: 10.1038/ngeo2487.
807 Portis, D. H., M. P. Cellitti, W. L. Chapman, and J. E. Walsh, 2006: Low-frequency variability
808 and evolution of North American cold air outbreaks. *Mon. Wea. Rev.*, **134,** 579–597, doi:
809 10.1175/MWR3083.1.
810 Ralph, F. M., P. J. Neiman, and G. A. Wick, 2004: Satellite and CALJET aircraft observations of
811 atmospheric rivers over the eastern North Pacific Ocean during the winter of 1997/98.
812 *Mon. Wea. Rev.*, **132,** 1721–1745, doi: 10.1175/1520-
813 0493(2004)132<1721:SACAOO>2.0.CO;2.
814 Riemer, M., S. C. Jones, and C. A. Davis, 2008: The impact of extratropical transition on the
815 downstream flow: An idealized modelling study with a straight jet. *Quart. J. Roy.*
816 *Meteor. Soc.*, **134**, 69–91, doi: 10.1002/qj.189.
817 Rogers, J. C., and R. V. Rohli, 1991: Florida citrus freezes and polar anticyclones in the Great
818 Plains. *J. Climate*, **4,** 1103–1113, doi: 10.1175/1520-0442(1991)004<1103:FCFAPA>
819 2.0.CO;2.

820 Saha, S., and Coauthors, 2010: The NCEP Climate Forecast System Reanalysis. *Bull. Amer.*
821 *Meteor. Soc.*, **91**, 1015–1057, doi: 10.1175/2010BAMS3001.1.
822 Saha, S., and Coauthors, 2014: The NCEP Climate Forecast System version 2. *J. Climate*, **27**,
823 2185–2208, doi: 10.1175/JCLI-D-12-00823.1.
824 Sanders, F. and J. R. Gyakum, 1980, Synoptic-dynamic climatology of the "bomb." *Mon. Wea.*
825 *Rev.*, **108,** 1589–1606, doi: 10.1175/1520-0493(1980)108<1589:SDCOT>2.0.CO;2.
826 Scherer, M., and N. S. Diffenbaugh, 2014: Transient twenty-first century changes in daily-scale
827 temperature extremes in the United States. *Climate Dyn.*, **42,** 1383–1404, doi:
828 10.1007/s00382-013-1829-2.
829 Tippett, M. K., J. T. Allen, V. A. Gensini, and H. E. Brooks, 2015: Climate and hazardous
830 convective weather. *Curr. Climate Change Rep.*, **1,** 60–73, doi: 10.1007/s40641-015-
831 0006-6.
832 Torn, R. D., 2010: Diagnosis of the downstream ridging associated with extratropical transition
833 using short-term ensemble forecasts. *J. Atmos. Sci.*, **67**, 817–833, doi:
834 10.1175/2009JAS3093.1.
835 Torn, R. D., and G. J. Hakim, 2015: Comparison of wave packets associated with extratropical
836 transition and winter cyclones. *Mon. Wea. Rev.*, **143**, 1782–1803, doi: 10.1175/MWR-D-
837 14-00006.1.
838 Turner, J. K., and J. R. Gyakum, 2011: The development of arctic air masses in northwest
839 Canada and their behavior in a warming climate. *J. Climate*, **24,** 4618–4633, doi:
840 10.1175/2011JCLI3855.1.

841 Vavrus, S., J. E. Walsh, W. L. Chapman, and D. Portis, 2006: The behavior of extreme cold air
842 outbreaks under greenhouse warming. *Int. J. Climatol.*, **26,** 1133–1147, doi:
843 10.1002/joc.1301.
844 Walsh, J. E., A. S. Phillips, D. H. Portis, and W. L. Chapman, 2001: Extreme cold outbreaks in
845 the United States and Europe, 1948–99. *J. Climate*, **14,** 2642–2658, doi: 10.1175/1520-
846 0442(2001)014<2642:ECOITU>2.0.CO;2.
847 Wilks, D. S., 2011: Statistical Methods in the Atmospheric Sciences. 3rd ed. Elsevier, 676 pp.
848 Winters, A. C., D. Keyser, and L. F. Bosart, 2018: The development of the North Pacific Jet
849 Phase Diagram as an objective tool to monitor the state of the upper-tropospheric flow
850 pattern. *Wea. Forecasting*, **33,** (in review).
851 Westby, R. M., Y.-Y. Lee, and R. X. Black, 2013: Anomalous temperature regimes during the
852 cool season: Long-term trends, low-frequency mode modulation, and representation in
853 CMIP5 simulations. *J. Climate*, **26,** 9061–9076, doi: 10.1175/JCLI-D-13-00003.1.
854 Westby, R. M., and R. X. Black, 2015: Development of anomalous temperature regimes over the
855 southeastern United States: Synoptic behavior and role of low-frequency modes. *Wea.*
856 *Forecasting*, **30,** 553–570, doi: 10.1175/WAF-D-14-00093.1.
857 Wolter, K., M. Hoerling, J. K. Eischeid, G. J. van Oldenborgh, X.-W. Quan, J. E. Walsh, T. N.
858 Chase, and R. M. Dole, 2015: How unusual was the cold winter of 2013/14 in the Upper
859 Midwest? *Bull. Amer. Meteor. Soc.*, **96,** S10–S14, doi: 10.1175/BAMS-D-15-00126.1.
860 Xie, Z., R. X. Black, and Y. Deng, 2017: Daily-scale planetary wave patterns and the modulation
861 of cold season weather in the northern extratropics. *J. Geophys. Res. Atmos.*, **122,** 8383–
862 8398, doi: 10.1002/2017JD026768.

Zhu, Y., and R. E. Newell, 1998: A proposed algorithm for moisture fluxes from atmospheric rivers. *Mon. Wea. Rev.*, **126,** 725–735, doi: 10.1175/1520-0493(1998)126<0725:APAFMF>2.0.CO;2.

Table Captions

TABLE 1. The minimum grid point thresholds required for the identification of an ETE within the eastern and western U.S. domains. The total number of ETEs identified during 1979–2014 within the eastern and western U.S. domains, as well as the number of ETEs that occurred during the cool season (Sep–May). Refer to the text for a full discussion of the ETE identification scheme.

Tables

Extreme Temperature Events				
	Spatial Domain	Min. Grid Point Threshold	Total Number of Identified Events	Cool Season Events
Extreme Warm Events	**East**	224	304	239
	West	144	264	204
Extreme Cold Events	**East**	221	225	173
	West	125	269	196

TABLE 1. The minimum grid point thresholds required for the identification of an ETE within the eastern and western U.S. domains. The total number of ETEs identified during 1979–2014 within the eastern and western U.S. domains, as well as the number of ETEs that occurred during the cool season (Sep–May). Refer to the text for a full discussion of the ETE identification scheme.

Figure Captions

FIG. 1. (a) Frequency distribution of 2-m temperatures compiled at 24-h intervals within a 21-day window centered on 1900 UTC 30 May for every year between 1979 and 2014 for a grid point near Albany, NY (43°N; –74°W). The vertical black bar identifies the 99th-percentile temperature of the distribution and the quantity in the top left of the panel indicates the total number of 1-h forecasts that are used to construct the distribution. (b) 99th-percentile temperature at 1900 UTC 30 May is shaded in the fill pattern. The black boxes identify the eastern and western U.S. domains used to identify continental U.S. ETEs. (c) Frequency distribution of the number of grid points characterized by extreme warmth within the subset of 1-h forecasts during 1979–2014 that exhibit at least one grid point over land in the eastern U.S. domain with a 2-m temperature greater than its respective 99th-percentile temperature. The vertical black bar identifies the number of grid points corresponding to the 95th percentile of the distribution. The short vertical black bar identifies the maximum number of grid points characterized by extreme warmth in a single 1-h forecast during 1979–2014.

FIG. 2. (a) The frequency of extreme warm event initiation within the eastern U.S. domain is shaded in the fill pattern. Individual extreme warm event centroids are represented by dots and are colored according to their respective geographic cluster. (b) As in (a), but for extreme warm event initiation within the western U.S. domain.

FIG. 3. As in Fig. 2, but for extreme cold event initiation within the (a) eastern U.S. domain and (b) western U.S. domain.

952 FIG. 4. (a) September–May 250-hPa mean zonal wind is contoured in black every 10 m s^{-1}
953 above 30 m s^{-1}, and the regression of EOF 1 onto 250-hPa zonal wind anomaly data is shaded in
954 m s^{-1}. (b) As in (a), but for EOF 2. Figure and caption from Winters et al. (2018).
955
956 FIG. 5. Schematic illustrating the NPJ Phase Diagram and the classification scheme used to
957 determine the NPJ regime prior to ETE initiation.
958
959 FIG. 6. Composite mean 250-hPa wind speed in m s^{-1} is shaded in the fill pattern, 250-hPa
960 geopotential height is contoured in black every 120 m, and 250-hPa geopotential height
961 anomalies are contoured in solid red and dashed blue every 30 m for positive and negative
962 values, respectively, 4 days following the initiation of a (a) jet extension, (b) jet retraction, (c)
963 poleward shift, and (d) equatorward shift regime. The numbers in the bottom right of each panel
964 indicate the number of cases included in each composite and stippled areas represent locations
965 where the 250-hPa geopotential height anomalies are statistically significantly different from
966 climatology at the 99% confidence level. Figure and caption from Winters et al. (2018).
967
968 FIG. 7. Composite anomalies of mean sea-level pressure are contoured in solid and dashed black
969 every 2 hPa for positive and negative values, respectively, and 850-hPa temperature anomalies
970 are shaded in the fill pattern every 1 K 4 days following the initiation of a (a) jet extension, (b)
971 jet retraction, (c) poleward shift, and (d) equatorward shift regime. The numbers in the bottom
972 right of each panel indicate the number of cases included in each composite and stippled areas
973 represent locations where the 850-hPa temperature anomalies are statistically significantly

974 different from climatology at the 99% confidence level. Figure and caption from Winters et al.
975 (2018).
976
977 FIG. 8. (a) The average position of the NPJ within the NPJ Phase Diagram 3–7 days prior to the
978 initiation of every eastern U.S. extreme warm event is identified with an 'x'. Individual x's are
979 colored by meteorological season according to the legend and the numbers in the legend identify
980 the number of ETEs within the eastern U.S. domain that initiated during each season. The
981 numbers in the black boxes identify the total number of x's that lie within each quadrant of the
982 NPJ Phase Diagram, while the numbers in the red, blue, and green boxes identify the number of
983 x's within that quadrant that are associated with ETEs that initiated during fall, winter, and
984 spring, respectively. As in (a), but for (b) Northern Plains, (c) Southern Plains, and (d) East
985 Coast extreme warm events.
986
987 FIG. 9. As in Fig. 8, but for (a) western U.S., (b) Pacific Northwest, (c) Northern Rockies, and
988 (d) Southwest extreme warm events.
989
990 FIG. 10. (a) Composite trajectory showing the evolution of the NPJ at 6-h intervals during the
991 10-day period prior to ETE initiation for all eastern U.S. extreme warm events and the three
992 eastern U.S. geographic clusters. All trajectories are colored by geographic cluster according to
993 the legend and begin at the origin of the NPJ Phase Diagram 10 days prior to ETE initiation. The
994 colored diamonds offset from the origin of the NPJ Phase Diagram correspond to the state of the
995 NPJ at the time of ETE initiation. (b) As in (a), but for all western U.S. extreme warm events and
996 the three western U.S. geographic clusters.

997

998 FIG. 11. As in Fig. 8, but for (a) eastern U.S., (b) Northern Plains, (c) Northeast, (d) Southern
999 Plains, and (e) Southeast extreme cold events.

1000

1001 FIG. 12. As in Fig. 8, but for (a) western U.S., (b) Pacific Northwest, (c) Northern Rockies, and
1002 (d) Southwest extreme cold events.

1003

1004 FIG. 13. As in Fig. 8, but for (a) eastern U.S. and (b) western U.S. extreme cold events.

1005

1006 FIG. 14. Composite synoptic-scale flow evolution prior to the initiation of a Southern Plains
1007 extreme warm event following a jet retraction. [left column] 250-hPa wind speed is shaded in m
1008 s^{-1} following the legend, 250-hPa geopotential heights are contoured in black every 12 dam,
1009 standardized 250-hPa geopotential height anomalies are contoured in solid and dashed yellow
1010 every 0.5σ for positive and negative values, respectively, and positive standardized precipitable
1011 water anomalies are shaded in green following the legend (a) 6 days, (c) 4 days, (e) 2 days, and
1012 (g) 0 days prior to ETE initiation. Stippled areas represent locations where the 250-hPa
1013 geopotential height anomalies are statistically significantly different from climatology at the 99%
1014 confidence level. [right column] Standardized 850-hPa temperature anomalies are shaded every
1015 0.5σ following the legend, mean sea-level pressure is contoured in black every 4 hPa, and 1000–
1016 500-hPa thickness is contoured in dashed red and blue for values greater than 540 dam or less
1017 than or equal to 540 dam, respectively, (b) 6 days, (d) 4 days, (f) 2 days, and (h) 0 days prior to
1018 ETE initiation. The red 'L's and blue 'H's identify the locations of surface cyclones and

anticyclones. Stippled areas represent locations where the 850-hPa geopotential height anomalies are statistically significantly different from climatology at the 99% confidence level.

Figures

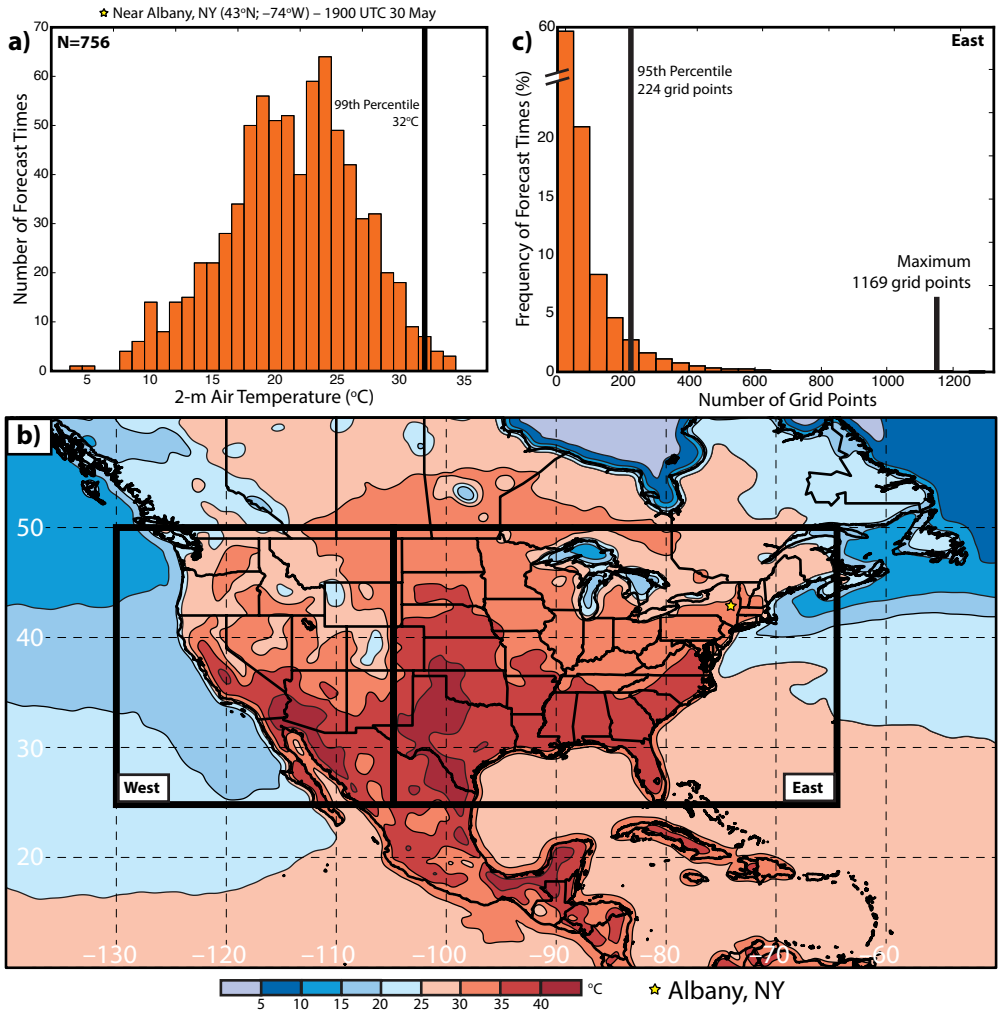

FIG. 1. (a) Frequency distribution of 2-m temperatures compiled at 24-h intervals within a 21-day window centered on 1900 UTC 30 May for every year between 1979 and 2014 for a grid point near Albany, NY (43°N; –74°W). The vertical black bar identifies the 99th-percentile temperature of the distribution and the quantity in the top left of the panel indicates the total number of 1-h forecasts that are used to construct the distribution. (b) 99th-percentile temperature at 1900 UTC 30 May is shaded in the fill pattern. The black boxes identify the eastern and western U.S. domains used to identify continental U.S. ETEs. (c) Frequency distribution of the number of grid points characterized by extreme warmth within the subset of 1-h forecasts during 1979–2014 that exhibit at least one grid point over land in the eastern U.S. domain with a 2-m temperature greater than its respective 99th-percentile temperature. The vertical black bar identifies the number of grid points corresponding to the 95th percentile of the distribution. The short vertical black bar identifies the maximum number of grid points characterized by extreme warmth in a single 1-h forecast during 1979–2014.

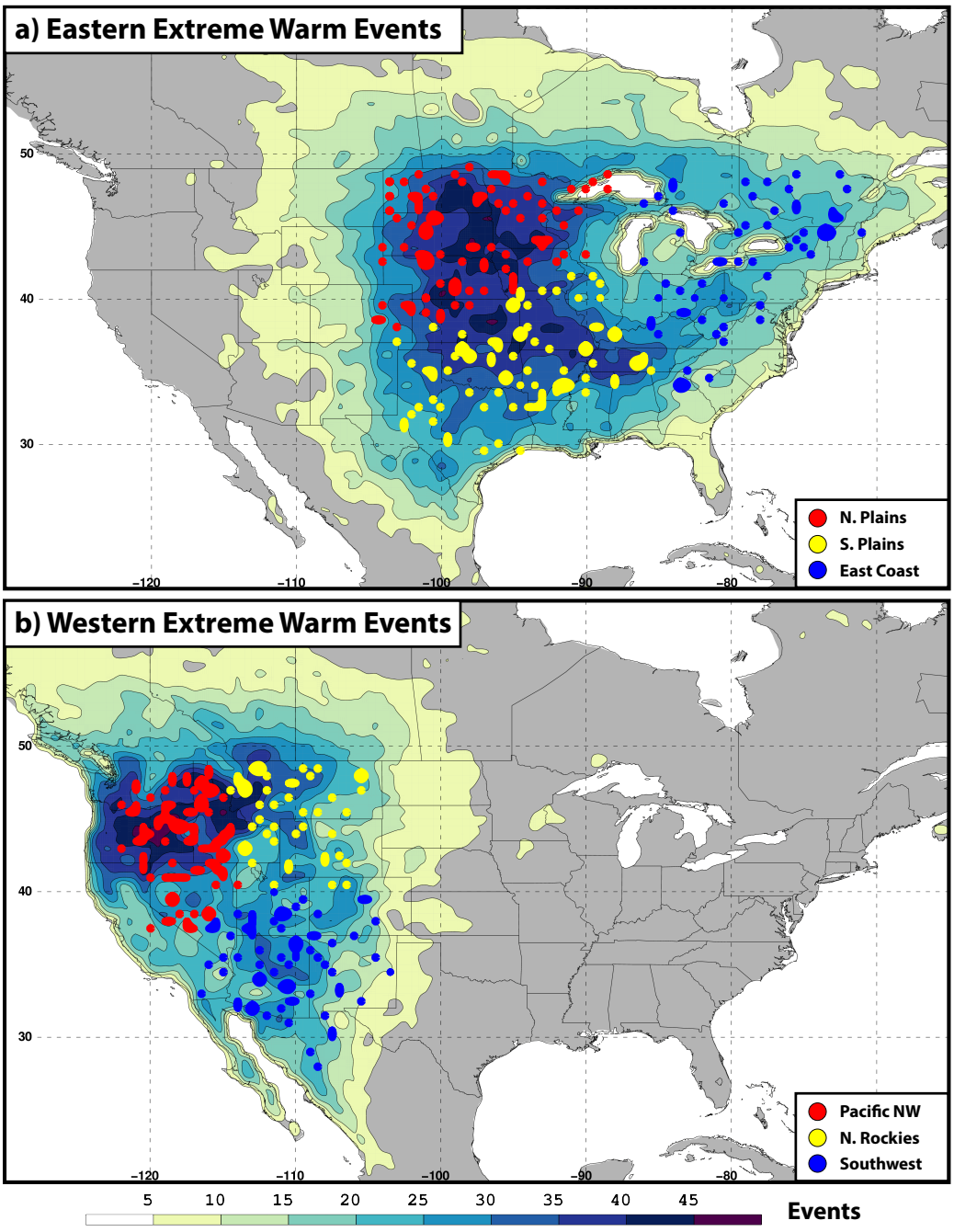

FIG. 2. (a) The frequency of extreme warm event initiation within the eastern U.S. domain is shaded in the fill pattern. Individual extreme warm event centroids are represented by dots and are colored according to their respective geographic cluster. (b) As in (a), but for extreme warm event initiation within the western U.S. domain.

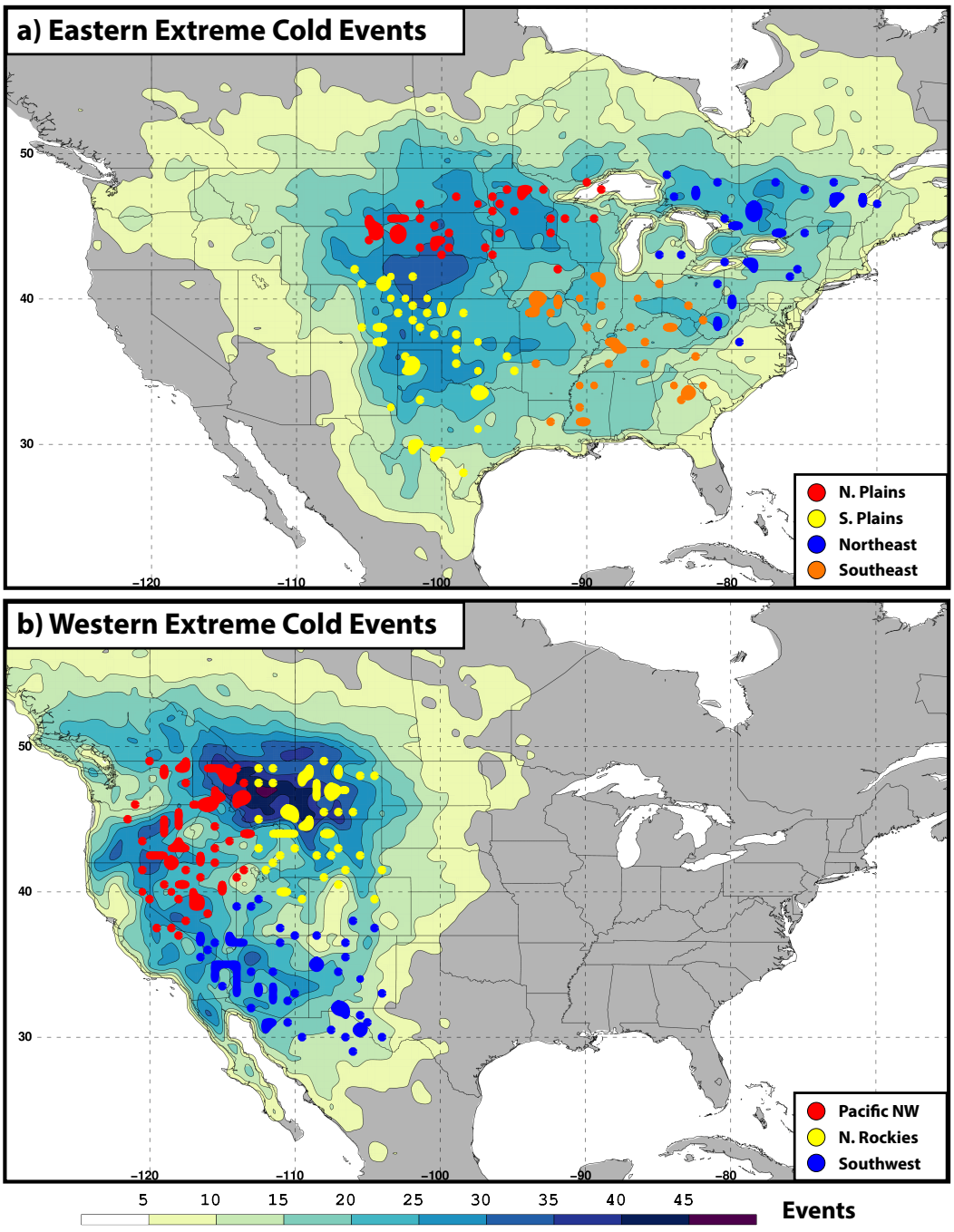

FIG. 3. As in Fig. 2, but for extreme cold event initiation within the (a) eastern U.S. domain and (b) western U.S. domain.

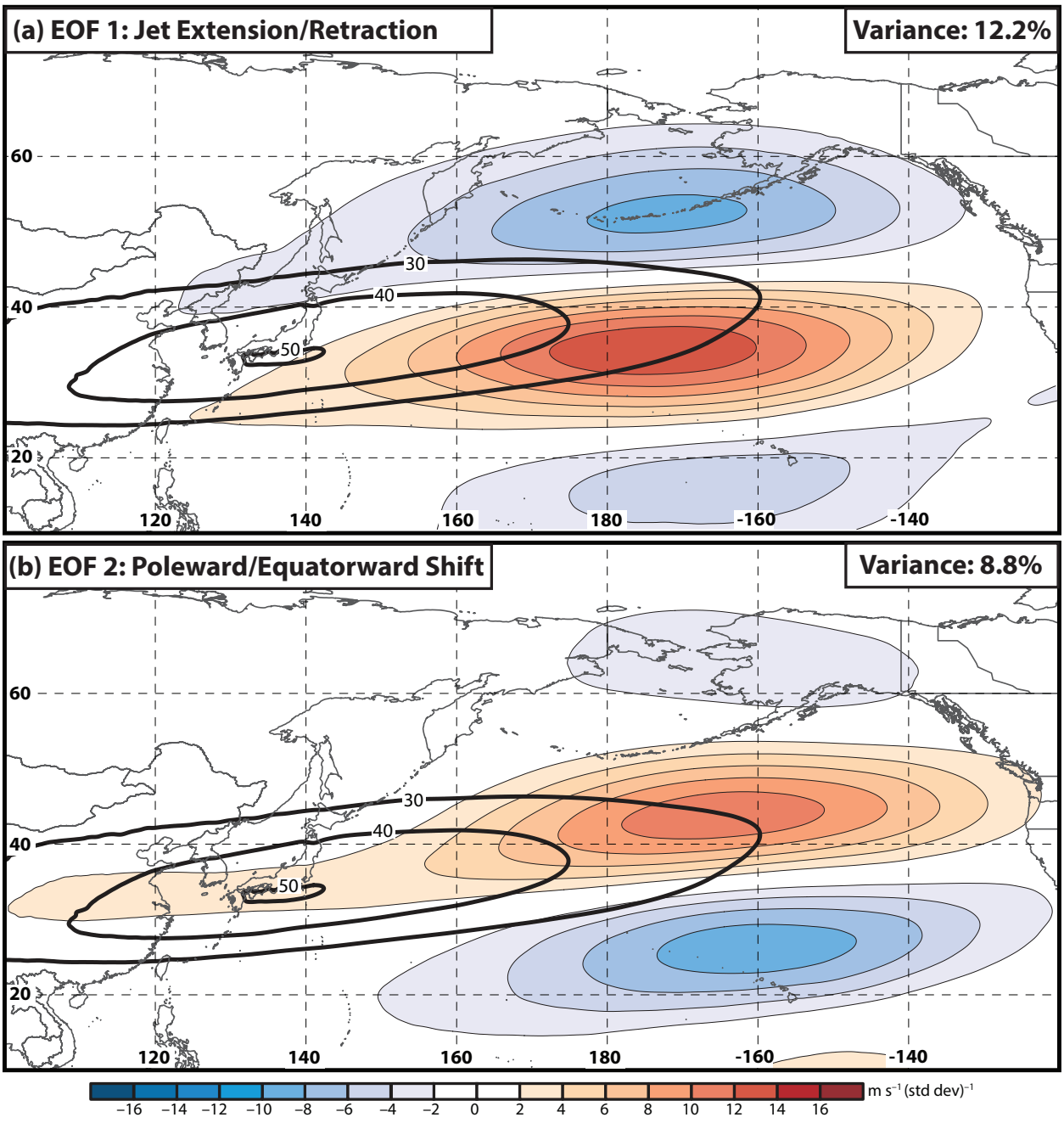

FIG. 4. (a) September–May 250-hPa mean zonal wind is contoured in black every 10 m s^{-1} above 30 m s^{-1}, and the regression of EOF 1 onto 250-hPa zonal wind anomaly data is shaded in m s^{-1}. (b) As in (a), but for EOF 2. Figure and caption from Winters et al. (2018).

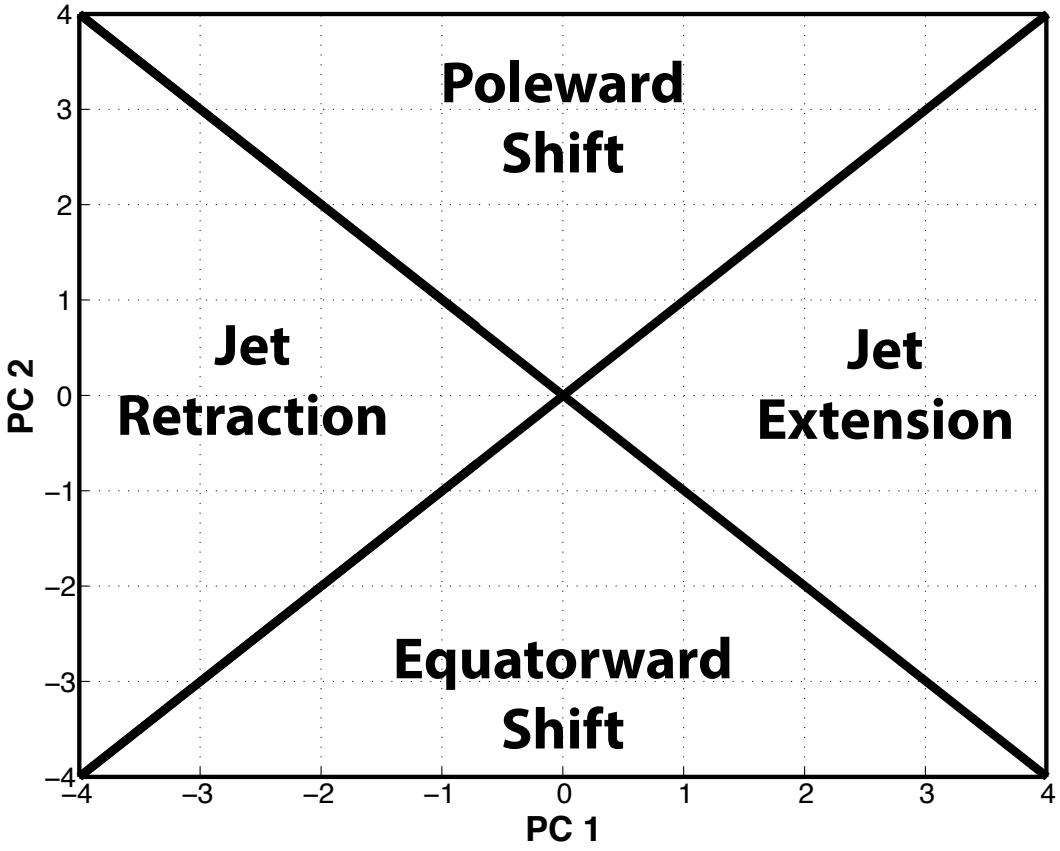

FIG. 5. Schematic illustrating the NPJ Phase Diagram and the classification scheme used to determine the NPJ regime prior to ETE initiation.

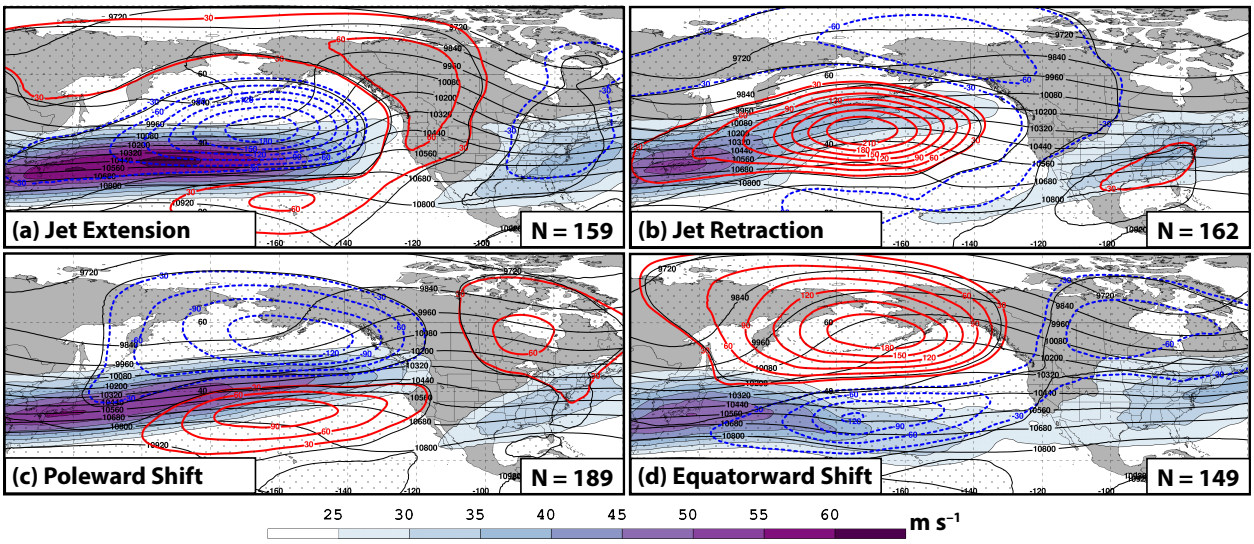

FIG. 6. Composite mean 250-hPa wind speed in m s^{-1} is shaded in the fill pattern, 250-hPa geopotential height is contoured in black every 120 m, and 250-hPa geopotential height anomalies are contoured in solid red and dashed blue every 30 m for positive and negative values, respectively, 4 days following the initiation of a (a) jet extension, (b) jet retraction, (c) poleward shift, and (d) equatorward shift regime. The numbers in the bottom right of each panel indicate the number of cases included in each composite and stippled areas represent locations where the 250-hPa geopotential height anomalies are statistically significantly different from climatology at the 99% confidence level. Figure and caption from Winters et al. (2018).

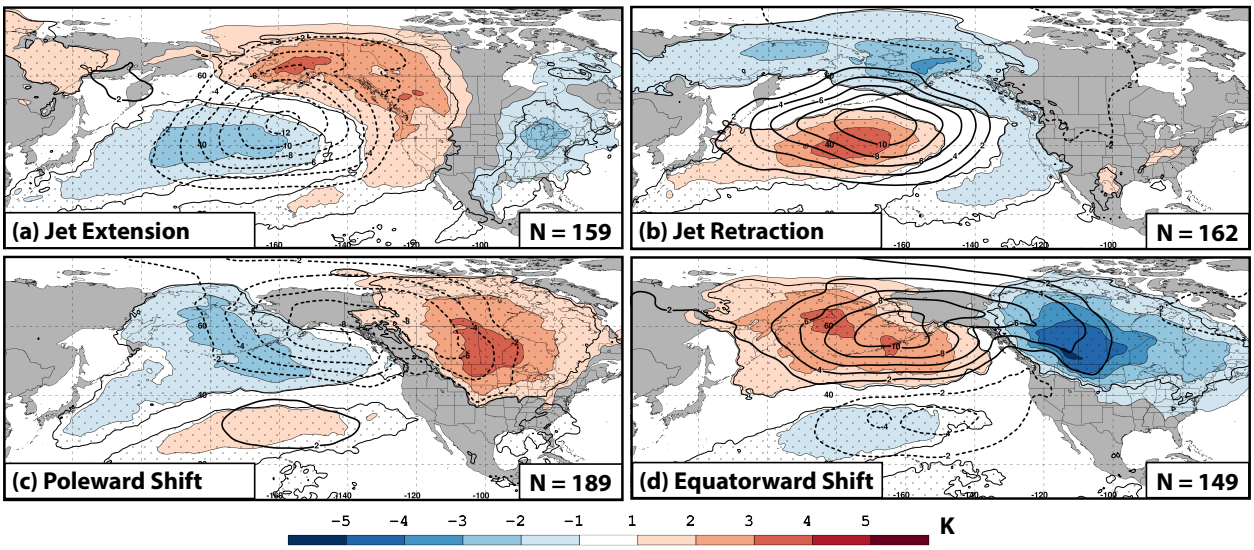

FIG. 7. Composite anomalies of mean sea-level pressure are contoured in solid and dashed black every 2 hPa for positive and negative values, respectively, and 850-hPa temperature anomalies are shaded in the fill pattern every 1 K 4 days following the initiation of a (a) jet extension, (b) jet retraction, (c) poleward shift, and (d) equatorward shift regime. The numbers in the bottom right of each panel indicate the number of cases included in each composite and stippled areas represent locations where the 850-hPa temperature anomalies are statistically significantly different from climatology at the 99% confidence level. Figure and caption from Winters et al. (2018).

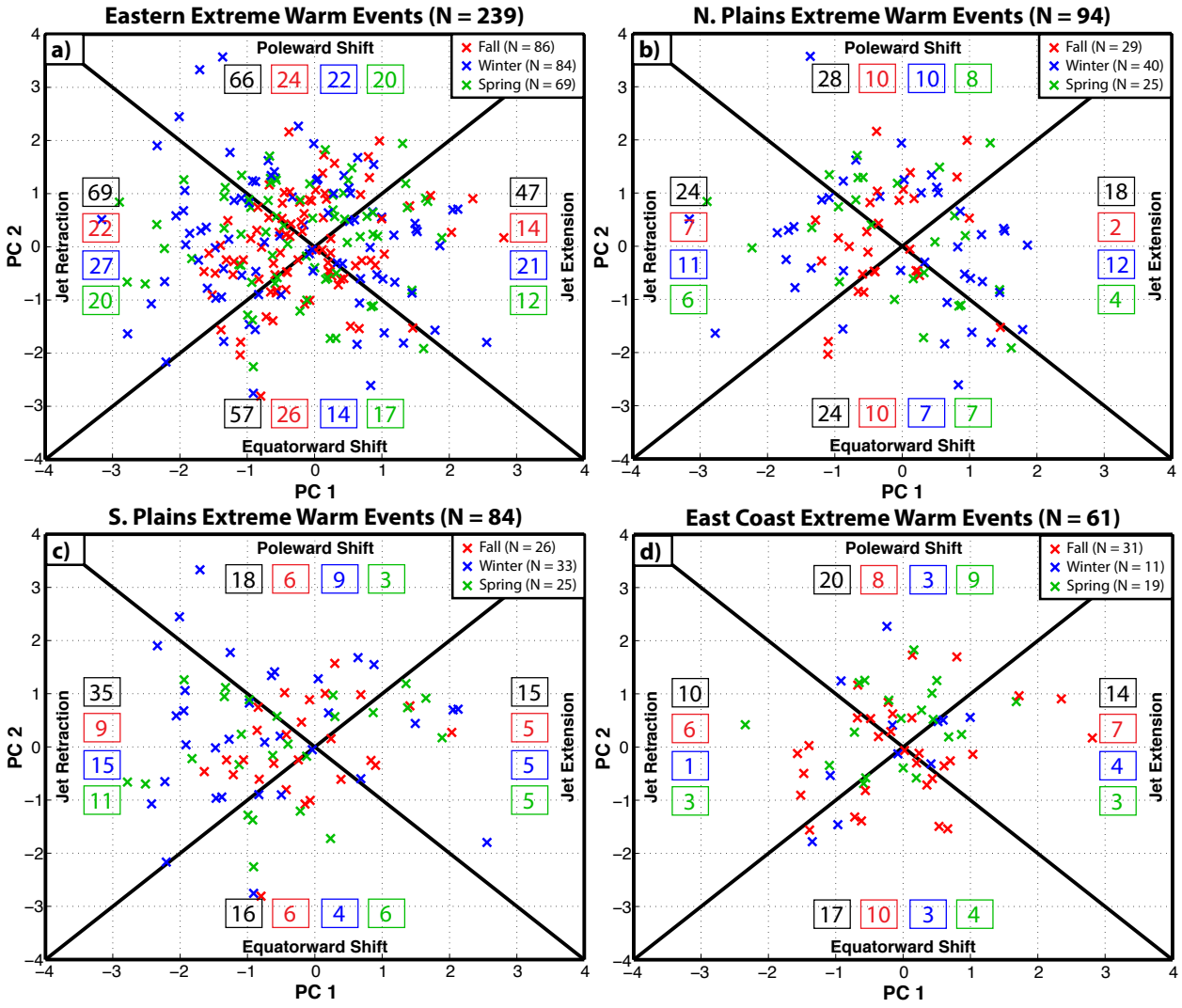

FIG. 8. (a) The average position of the NPJ within the NPJ Phase Diagram 3–7 days prior to the initiation of every eastern U.S. extreme warm event is identified with an ‘x’. Individual x’s are colored by meteorological season according to the legend and the numbers in the legend identify the number of ETEs within the eastern U.S. domain that initiated during each season. The numbers in the black boxes identify the total number of x’s that lie within each quadrant of the NPJ Phase Diagram, while the numbers in the red, blue, and green boxes identify the number of x’s within that quadrant that are associated with ETEs that initiated during fall, winter, and spring, respectively. As in (a), but for (b) Northern Plains, (c) Southern Plains, and (d) East Coast extreme warm events.

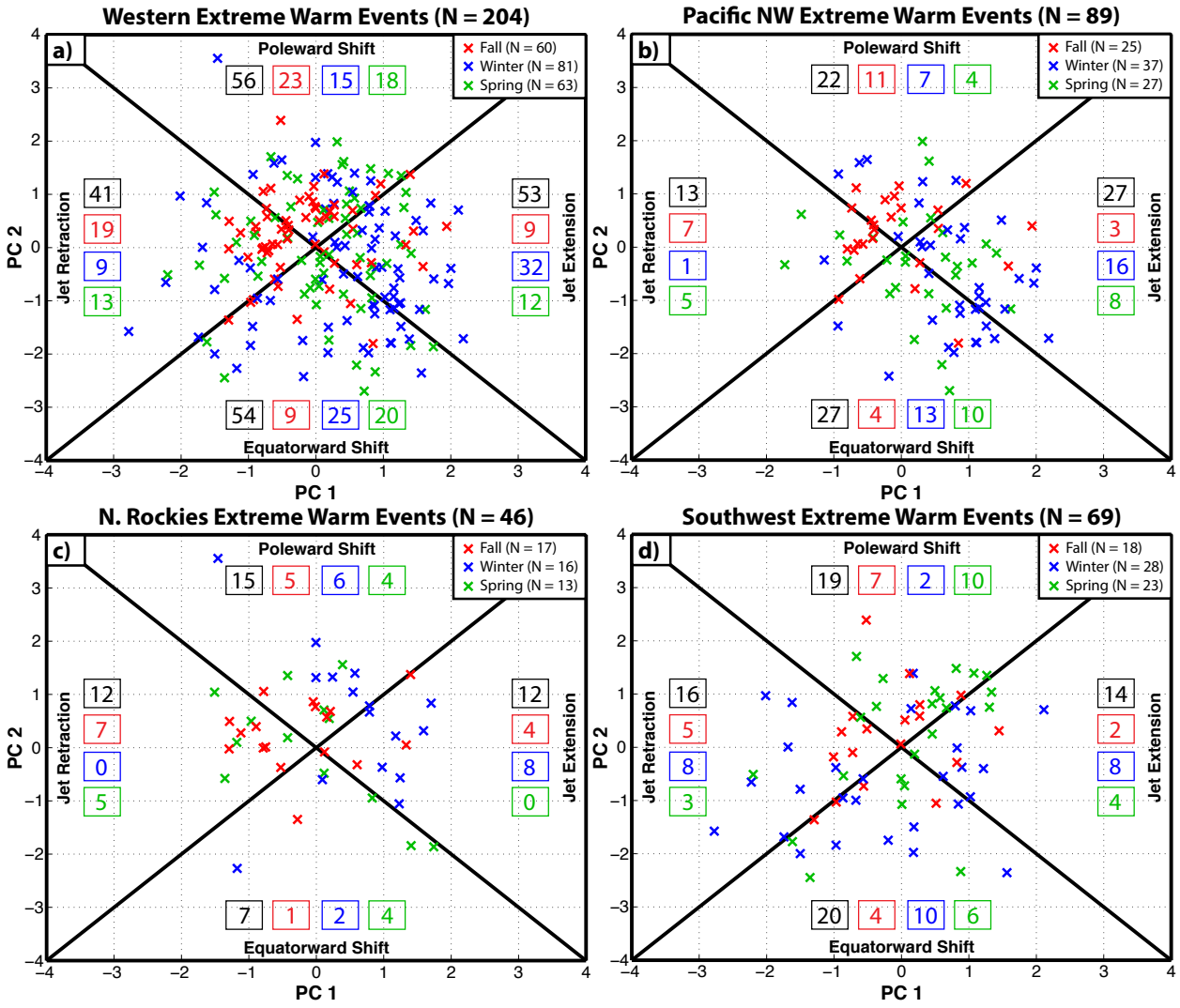

FIG. 9. As in Fig. 8, but for (a) western U.S., (b) Pacific Northwest, (c) Northern Rockies, and (d) Southwest extreme warm events.

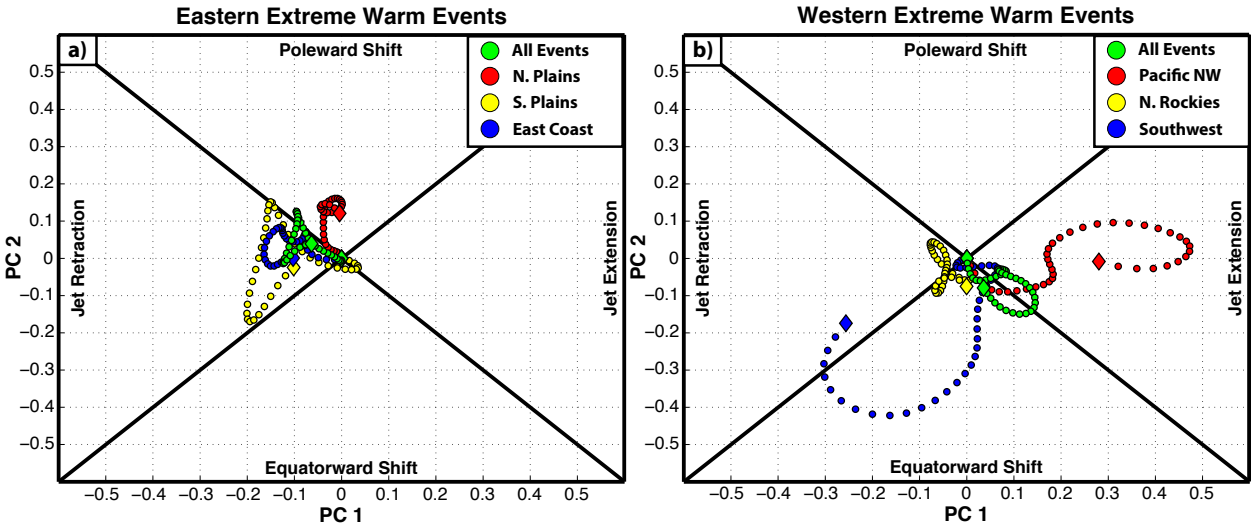

FIG. 10. (a) Composite trajectory showing the evolution of the NPJ at 6-h intervals during the 10-day period prior to ETE initiation for all eastern U.S. extreme warm events and the three eastern U.S. geographic clusters. All trajectories are colored by geographic cluster according to the legend and begin at the origin of the NPJ Phase Diagram 10 days prior to ETE initiation. The colored diamonds offset from the origin of the NPJ Phase Diagram correspond to the state of the NPJ at the time of ETE initiation. (b) As in (a), but for all western U.S. extreme warm events and the three western U.S. geographic clusters.

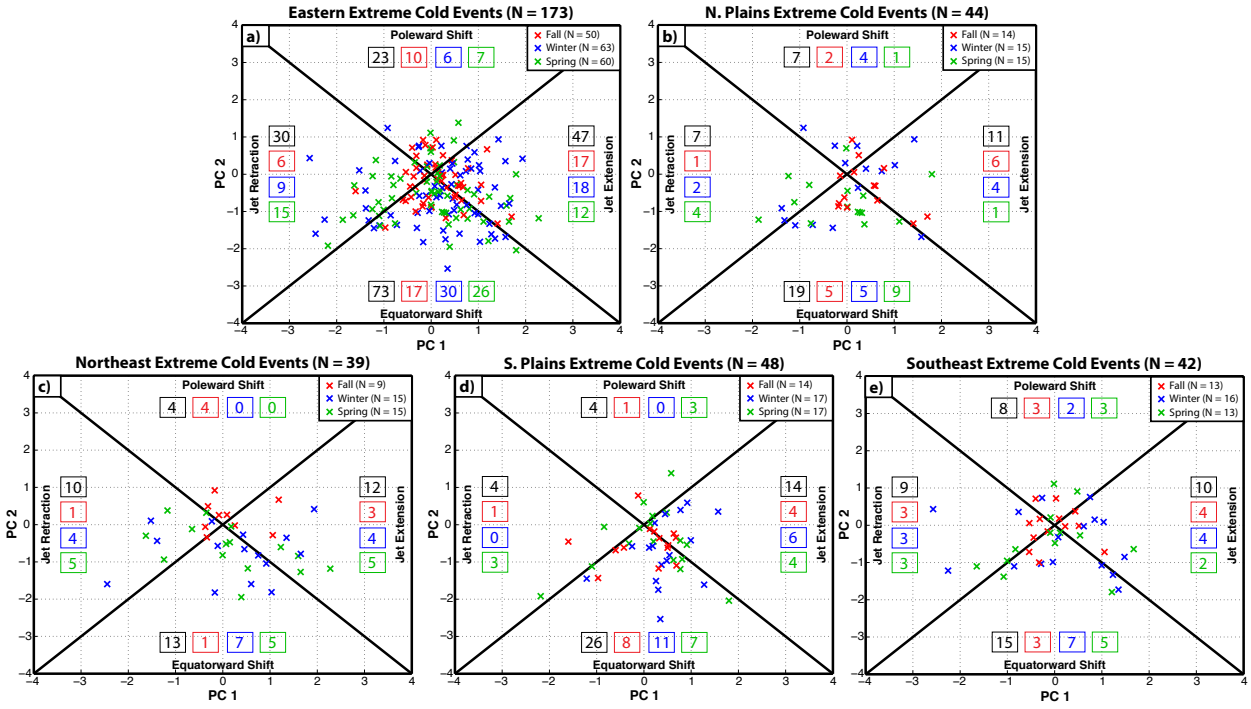

FIG. 11. As in Fig. 8, but for (a) eastern U.S., (b) Northern Plains, (c) Northeast, (d) Southern Plains, and (e) Southeast extreme cold events.

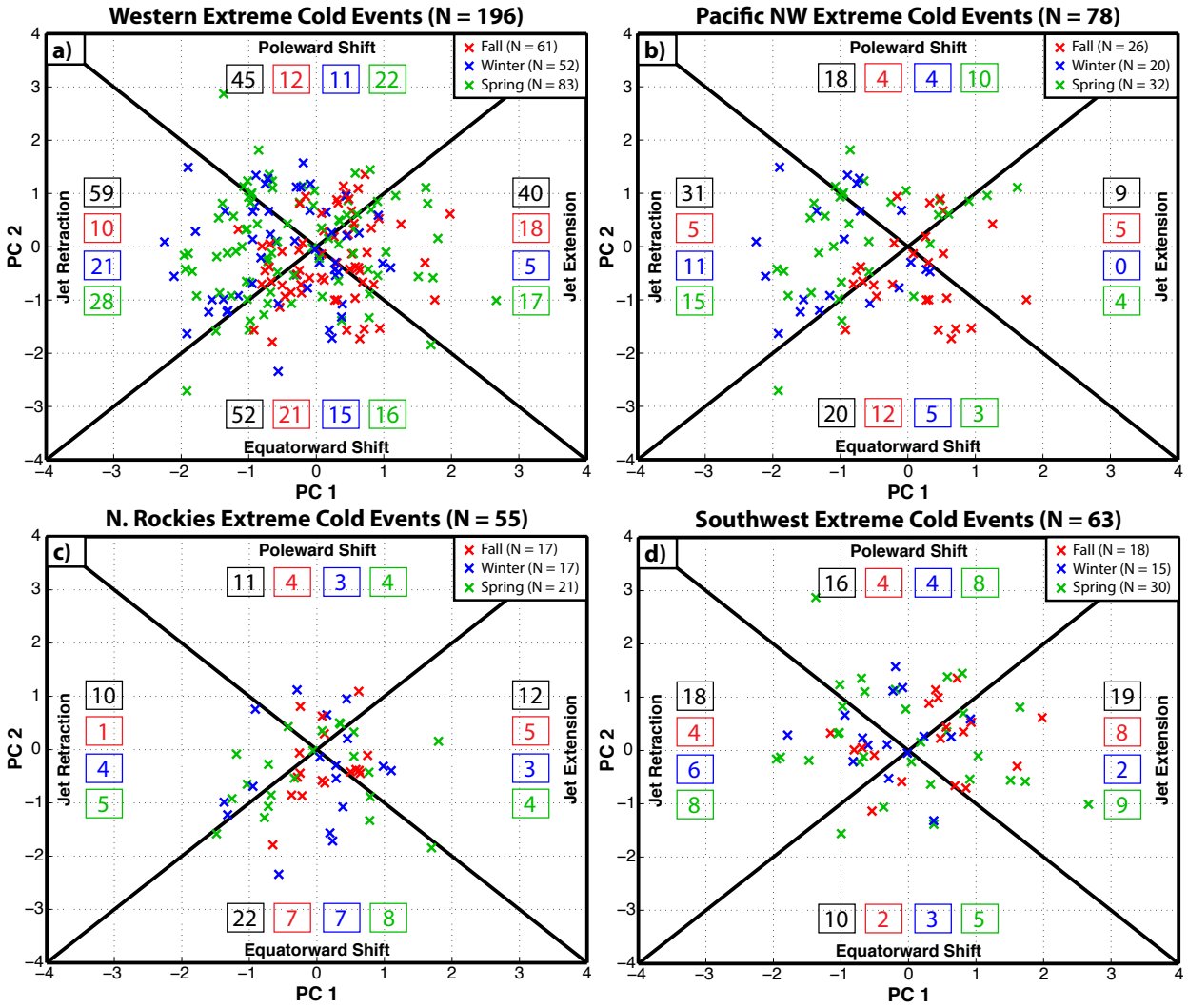

FIG. 12. As in Fig. 8, but for (a) western U.S., (b) Pacific Northwest, (c) Northern Rockies, and (d) Southwest extreme cold events.

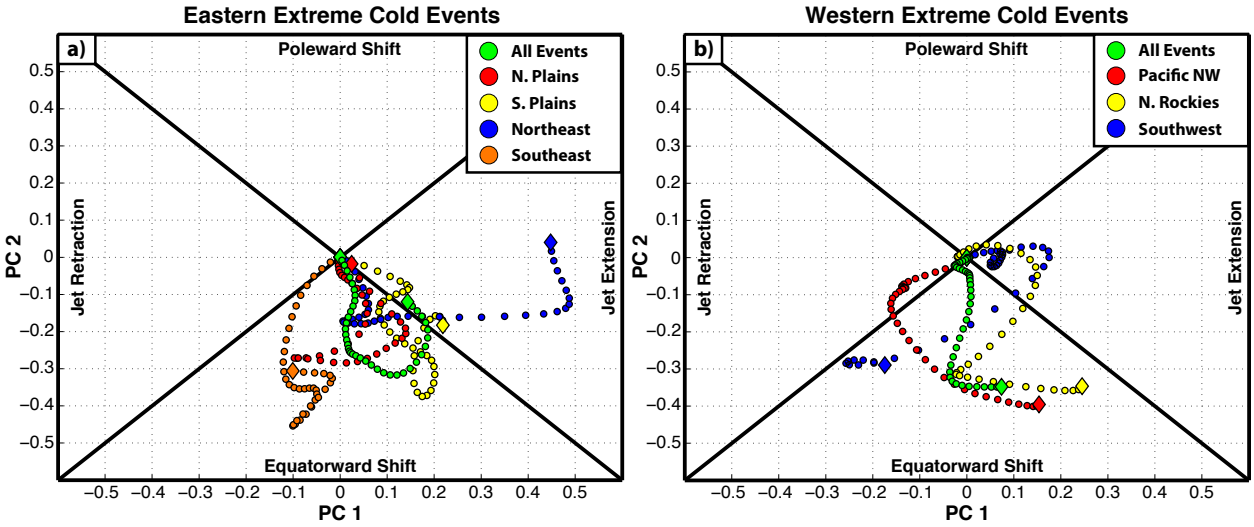

FIG. 13. As in Fig. 8, but for (a) eastern U.S. and (b) western U.S. extreme cold events.

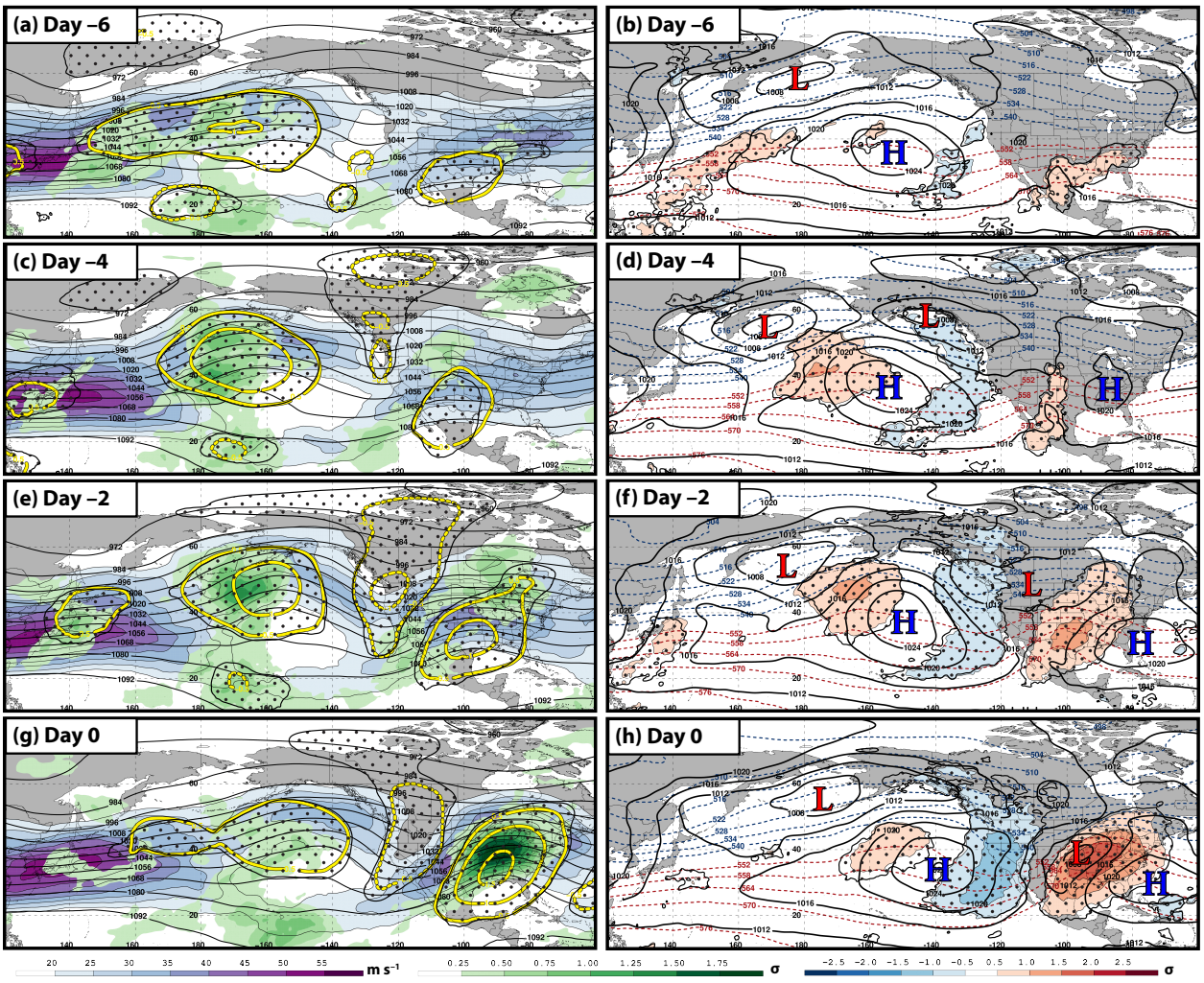

FIG. 14. Composite synoptic-scale flow evolution prior to the initiation of a Southern Plains extreme warm event following a jet retraction. [left column] 250-hPa wind speed is shaded in m s^{-1} following the legend, 250-hPa geopotential heights are contoured in black every 12 dam, standardized 250-hPa geopotential height anomalies are contoured in solid and dashed yellow every 0.5σ for positive and negative values, respectively, and positive standardized precipitable water anomalies are shaded in green following the legend (a) 6 days, (c) 4 days, (e) 2 days, and (g) 0 days prior to ETE initiation. Stippled areas represent locations where the 250-hPa geopotential height anomalies are statistically significantly different from climatology at the 99% confidence level. [right column] Standardized 850-hPa temperature anomalies are shaded every 0.5σ following the legend, mean sea-level pressure is contoured in black every 4 hPa, and 1000–500-hPa thickness is contoured in dashed red and blue for values greater than 540 dam or less than or equal to 540 dam, respectively, (b) 6 days, (d) 4 days, (f) 2 days, and (h) 0 days prior to ETE initiation. The red 'L's and blue 'H's identify the locations of surface cyclones and anticyclones. Stippled areas represent locations where the 850-hPa geopotential height anomalies are statistically significantly different from climatology at the 99% confidence level.